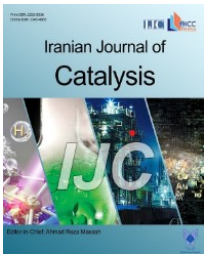

Iran. J. Catal. 2026; 16(1): 101-126

Iranian Journal of Catalysis (IJC)

https://doi.org/10.57647/ijc.2026.1601.07

Research Article

Eco-Friendly Fabrication of Ag-Ni Bimetallic Nanocatalyst for Catalytic Reduction of 4-Nitrophenol and Photodegradation of Crystal Violet Dye with Antibacterial Applications

Minakshi N. Bhatu[1,2], Guruprasad R. Mavlankar[1], Akshay Chavan[1], Prajakta P. Baikar[1], Dipali S. Raut[1], Shubhangi P. Patil[1,*]

[1] *Department of Chemistry, The Institute of Science, 15, Madam Cama Road, Mantralaya, Fort, Mumbai, Maharashtra, India*
[2] *Annasaheb Vartak College of Arts, Kedarnath Malhotra College of Commerce, E. S. Andrades, College of Science, Vasai Road, (west) Dist-Palghar Maharashtra, India*

[*] **Corresponding authors:** shubhangi.patil@iscm.ac.in

Article History:

Received:
30 October 2025

Revised:
6 November 2025

Accepted:
20 November 2025

Published Online:
1 December 2025

Published in Issue:
31 March 2026

Abstract

The facile and efficient green method for the synthesis of Ag based bimetallic nanoparticles Ag-Ni is developed by using sprout water extract. The phytochemical present in the sprout water extract assist the reduction of both the metal simultaneously according to their reduction potential and provides the way for seedless, one pot green synthesis. In the present study sprout water was used for the synthesis of Ag, Ni monometallic and bimetallic $Ag_{25}Ni_{75}$, $Ag_{50}Ni_{50}$, $Ag_{75}Ni_{25}$ because synergistic effect of two metal provides enhancement in catalytic properties of bimetallic nanoparticles. The synthesized nanocatalyst were further characterized by UV-visible analysis, XRD, EDX, NTA, TEM. The nanocatalyst is used for the reduction of organic pollutants like degradation of crystal violet dye and 4-nitrophenol. The nanoparticles were investigated for their antibacterial activity against Bacillus subtilis, staphylococcus aureus, Salmonella typhi, Pseudomonas aeruginosa, and Escherichia coli. The $Ag_{25}Ni_{75}$ shows outstanding performance for the reduction of 4-Nitrophenol. It will reduce 84.69 % of 4- nitrophenol just in 60 second with constant 0.70 min^{-1}. The order of the reaction is pseudo first order. The $Ag_{75}Ni_{25}$ shows excellent efficiency for the degradation of 66.37% crystal violet dye in 3 hrs following pseudo first order reaction with rate constant 0.007733min^{-1}. The $Ag_{75}Ni_{25}$ exhibits more zone of inhibition in *B. subtilis, S. aureus, S. typhi, P. aeruginosa,* and *E. coli* 15.36 ± 0.28 mm, 15.23 ± 0.15 mm, 15.40 ± 0.20 mm, 15.33± 0.23 mm, 15.40 ± 0.20 mm than monometallic silver and nickel.

Keywords: Antibacterial activity; Bimetallic nanoparticles; Crystal violet dye degradation; Green synthesis; Organic pollutants; Pseudo first order kinetic; 4-Nitrophenol reduction

Cite this article: M. N. Bhatu, G. R. Mavlankar, A. Chavan, P.P. Baikar, D. S. Raut, S. P., Patil. Iran. J. Catal. **16** (2026) 101-126.
https://doi.org/10.57647/ijc.2026.1601.07

1. Introductions

In recent years, the research community has shown increased interest in transforming toxic organic waste found in water into recyclable products that exhibit significantly reduced toxicity [1]. One of the main classes of harmful organic pollutants that is widely present in industrial and agricultural effluent is 4-nitrophenol (4-NP) and organic dyes [2]. The U.S. Environmental Protection Agency (EPA), states that 4-NP is one of the most harmful pollutants since short-term inhalation of the substance can result in headache, nausea, cyanosis, and drowsiness [2–4]. Effective removal of 4-NP has been also targeted using a number of techniques, including microwave-assisted catalytic degradation, photocatalytic processes, microorganism decomposition, and electrochemical oxidation approaches [2, 5–9]. Utilizing a suitable catalyst to reduce 4-NP by $NaBH_4$ is the most straightforward and environmentally beneficial way [2, 10–12]. Interestingly, the same reduction product, 4-aminophenol (4-AP), with a low toxicity character, has commercially valuable in various applications, such as drying agents, corrosion inhibition, anticorrosion lubricants, and photographic processing [1, 2, 13, 14].The degradation of dye are becoming difficult day by day. The factor responsible behind this difficulty are bigger size, complex structure and it's biodegradable structure. In industry the most commonly used dyes derivatives are anthraquinone, azo, phthalocyanine and indigoid derivatives [15–17]. It exerts various hazardous effects on human life like digestive tract irritation, skin irritation, respiratory, and kidney failure, etc. Several photocatalytic systems have been reported for degradation of 4-nitrophenol and crystal violet dye. ZnO supported on nano-clinoptilolite zeolite has shown excellent photocatalytic activity for 4-nitrophenol degradation through enhanced surface area and charge separation [18, 19]. Similarly, CdS nanoparticles embedded on zeolite A demonstrated efficient sunlight-assisted photodecolorization of crystal violet[cite new ref]. However, these systems often require expensive supports or toxic materials (CdS). Our Ag-Ni bimetallic system offers an eco-friendly alternative synthesized using non-toxic biological extracts while achieving comparable or superior catalytic activity.

Recently noble metal nanoparticle-based heterogeneous catalysts catched the attention of many people because of their potential for magnificent catalytic activity against hazardous organic contaminants[20–25]. The increased catalytic activity of nobel metal nanoparticles like silver because of their extraordinary physiochemical properties, which primarily comprise 1) Ag NP's easy control of catalytic activity through modification of their temperature, shape, and particle size [26] 2) Ag NPs catalysts are operating at ambient temperature or in mild conditions [27] 3) Because of their low cost the price of silver is 50 times lesser than Au or Pt similarly it is 25 times lesser than Pd which will makes Ag NP's catalysts are especially well-suited for real-world uses [28, 29] 4) A great environmental application value is provided by Ag NP's catalysts due to their low toxicity[30–32]. Despite being the ideal catalyst for $NaBH_4$ assisted 4-NP reduction, Ag NPs have a number of disadvantages when used alone, such as limited catalytic activity, poor stability, and quick oxidation and aggregation [30, 33]. Ag NP's catalytic properties have been reported to be significantly influenced by their size, shape, support, and composition. In order to enhance the catalytic property, three methods have been documented so far[30, 34]. First incorporating of Ag NP's into a range of substrates can successfully reduce the aggregation of these particles, increasing their catalytic activity. This is made possible due to the high interaction between Ag NP's and their support [35, 36]. Second, anisotropic Ag NP's are employed in place of conventional spherical Ag NP's because they have more active surface sites and The sharp angles and edges of the small molecule reactants make it easier for them to be absorbed on their surface [37, 38]. Third, bimetallic catalytic systems have lately been popular in order to tune the composition effects because of their increased activity due to synergistic effect, selectivity, cost effective nature as well as stability for longer time [39]. Thus, different approaches have been constructed to address the aforementioned problems, and Making Ag-based nanocomposites, especially supported and bimetallic Ag nanocomposites, is one successful endeavour [30, 35, 40]. Nanoclusters of Au_{25}, nanoclusters of Pd, nanocrystalline of Pt-CeO_2, Ag nanoparticles, bimetallic nanoparticles of Au-Ag, bimetallic nanocrystals of Pd/Au and nanoparticles of Au-Pt are a few examples [41–46]. However, the above noble metals' high price and low abundance, or that of their bimetallic counterparts, severely limit their practical usage [47]. For the hydrogenation of 4-NP, Cu, Co, and Ni transition metal and it's oxides becoming quite popular recently [48–51]. Nickel can fine-tune optical properties by increasing absorption of visible light which assisted by decreasing recombination of charge carrier. This is possible through the impurity level which is present in between the conduction bands and valence bands [52]. Despite the promising potential of heterogeneous photocatalysis for environmental remediation, several fundamental challenges remain [53, 54].

The primary limitation is the rapid recombination of photogenerated electron-hole pairs (typically within nanoseconds), which drastically reduces quantum efficiency to < 10% in most photocatalysts. Additional challenges include: (i) limited visible light absorption (most wide-band gap semiconductors only absorb UV), (ii) photo-corrosion and stability issues, (iii) difficulty in catalyst recovery from aqueous systems, and (iv) toxicity

10.57647/ijc.2026.1601.07

concerns for many high-performance photocatalysts containing Cd, Pb, or other heavy metals.

To address these challenges, various strategies have been developed including: heterojunction formation (type-II, Z-scheme), noble metal loading for plasmonic enhancement and electron sinks, doping to narrow band gap, and morphology engineering to increase surface area. Bimetallic systems, particularly those combining noble metals with transition metals, offer a promising approach by synergistically combining plasmonic effects, charge separation, and catalytic active sites [53, 55].

In addition to environmental pollution by organic contaminants, water contamination by pathogenic bacteria poses a serious threat to public health. An ideal water treatment material should address both chemical pollutants and biological contaminants simultaneously. Bimetallic Ag-Ni nanoparticles are particularly promising in this context because silver is well-known for its broad-spectrum antibacterial activity while nickel enhances catalytic performance.

Therefore, evaluating both pollutant degradation and antibacterial activity in the same material provides a comprehensive assessment of its potential for practical water treatment applications.

This work presents several novel contributions (1) First green synthesis of Ag-Ni bimetallic nanoparticles using chickpea sprout water extract as reducing/stabilizing agent; (2) Comprehensive compositional study revealing $Ag_{25}Ni_{75}$ as optimal for 4-NP reduction (84.69% degradation in 60 s, k = 0.0117 min^{-1}), among the fastest reported for Ag-Ni catalysts; (3) Dual application assessment both catalytic (4-NP reduction) and photocatalytic (CV degradation) using identical catalyst (4) True green synthesis without toxic reducing agents at ambient conditions (60 °C, 1 atm); (5) Multifunctional platform integrating catalytic, photocatalytic, and antibacterial activities; (6) Economic feasibility with inexpensive chickpea sprouts as starting material, making large-scale production viable. These advantages collectively position this work as a significant advance in sustainable nanomaterial development for environmental remediation [1, 56–58].

In present research article we try to focussed on the eco-friendly method for the designing of Ag based bimetallic nanoparticles hence we select sprout water extract as agent to synthesized Ag-Ni bimetallic nanoparticles. The two organic pollutants are targeted for degradation by using above synthesized bimetallic and monometallic nanoparticles. The first pollutant under consideration is of 4 – NP and second is crystal violet dye (CV). This study also includes kinetic study of degradation reactions and the biological activity like antibacterial applications. Its also help for the comparative study of bimetallic and monometallic nanoparticle towards degradation of 4-NP, crystal violet dye and antibacterial activity.

2. Material and methods

2.1. Chemicals

Silver nitrate ($AgNO_3$), Nickel (II) hexahydrate [$Ni(NO_3)_2.6H_2O$], 4-nitrophenol (4-NP) and sodium borohydride ($NaBH_4$) were purchased from Loba chem, India. All chemical reagents used in the research were freshly prepared (analytical grade) before performing the experiment.

To the authors' knowledge, this is the first application of chickpea sprout water extract for synthesis of Ag-Ni bimetallic nanoparticles.

2.2. Preparation of sprout water extract (SWE)

After thoroughly washing 100 g of chickpeas in look warm water to get rid of any contaminants, soak them in 300 ml of distilled water for a whole day. To remove insoluble impurities, we used Whatman Filter Paper No. 41 through which above water was filtered and the filtrate was collected in a 500 ml beaker, transfer it to a glass container and keep it in the refrigerator.

2.2.1. *Characterization of Sprout Water Extract*

The sprout water extract was characterized by FTIR spectroscopy to identify the phytochemicals present. The extract was freeze-dried and the dried powder was analyzed using FTIR in the range of 400-4000 cm^{-1}.

2.3. Monometallic Ag, Ni, and bimetallic Ag-Ni nanoparticle synthesis

The Ag-Ni bimetallic nanoparticles were synthesised by one pot green synthesis by applying seedless synthesis method at ambient temperature. In a typical synthesis, for each sample, the 2mM aqueous solution of silver and nickel precursor was taken ($AgNO_3$) silver nitrate and ($Ni(NO_3)_2.6H_2O$) Nickel nitrate hexahydrate by varying the volume (50 ml) maintaining the total molar intensity constant.

The Precursor solutions of silver nitrate ($AgNO_3$) and Nickel nitrate hexahydrate $Ni(NO_3)_2.6H_2O$ (2 mM) were combined in a single-neck flask with a glass stopper covering the top opening. The mixture was continuously stirred at 60^0C for approximately 60 minutes with the help of a magnetic stirrer. The 2.5 ml of aqueous SWE extract was added dropwise to the mixture of silver nitrate and nickel nitrate hexahydrate present in the glass stopper bottle with continuous stirring.

After the addition of SWE to the solution present in the stopper bottle changed from colourless to dark brown. This change in colour indicate the fabrication of Ag-Ni nanoparticles.

10.57647/ijc.2026.1601.07

Table 1. The compositions of prepared samples

Sample	$AgNO_3$ (2mM) (ml)	$Ni(NO_3)_2.6H_2O$ (2mM) (ml)	Ag:Ni
Ag	50	-	4 : -
$Ag_{25}Ni_{75}$	12.5	37.5	1:3
$Ag_{50}Ni_{50}$	25	25	2:2
$Ag_{75}Ni_{25}$	37.5	12.5	3:1
Ni	-	50	- : 4

Figure 1. synthesis of nanocatalyst (a) Ag_{100} (b) $Ag_{25}Ni_{75}$ (c) $Ag_{50}Ni_{50}$ (d) $Ag_{75}Ni_{25}$ (e) Ni_{100}

After the formation of Ag- Ni nanoparticles the solutions present in glass stopper bottle was taken in centrifugation tube and centrifuged for 20 minutes at 12,000 rpm to produce to settle down the Ag-Ni precipitate. Once the Ag-Ni precipitate gets settled it is washed with deionized water three times and followed by two hours of drying in a furnace set at 80^0C.

This process of drying gives rise to the brown powder of Ag-Ni bimetallic nanoparticles. $Ag_{50}Ni_{50}$, $Ag_{75}Ni_{25}$ NPs, and $Ag_{25}Ni_{75}$ NPs were the three Ag-Ni bimetallic samples that were synthesised; the suffix indicates the percentage. In addition, two monometallic samples were prepared under identical conditions for comparison: Ag NPs and Ni NPs. The preparation samples' components are displayed in Table 1. and images are shown in Fig. 1.

2.4. Characterisation of bimetallic nanoparticles

The Formation of monometallic Ag, Ni, and bimetallic Ag-Ni nanoparticles was confirmed by UV-Visible absorption spectroscopy using a UV-2450 SHIMADZU double beam spectrophotometer. Monometallic Ag, Ni, and bimetallic Ag-Ni of varying mass ratios were examined for crystallinity and phase structure using a powder X-ray diffraction pattern (XRD) captured on a X-rayX-ray diffractometer with a radiation source Cu Kα at ambient temperature, with 2θ ranging from 5 to 80^0. Fourier transform infrared spectroscopy (FTIR) was utilized to investigate the different functional groups of produced nanoparticles, utilizing wave numbers ranging from 400 to 4000 cm-1. To determine the composition of the synthesized nanoparticles, energy-dispersive X-ray spectroscopy (EDX) was utilized. The transmission electron microscope (TEM) assists in determining the microstructure and morphology, and a nanoparticle tracking analyzer (NTA) was employed to evaluate the size of nanoparticles.

2.5. Catalytic Activity Evaluation of 4-nitrophenol and crystal violet dye

The ability of the synthesized Ag, Ni, and Ag-Ni nanoparticles with varying compositions to reduce 4-nitrophenol and crystal violet dye was evaluated. The process of evaluating the catalytic activity for transforming 4-NP into 4-AP was conducted according to the documented method in the presence of $NaBH_4$ and also involved the synthesis of monometallic Ag, Ni, and varying compositions of bimetallic Ag-Ni. The oxidation-reduction reaction was carried out in a 3 ml quartz cuvette. The path length of the quartz cuvette is 1 cm. This was used as a batch reactor. In the cuvette, first 1.5 ml of light-yellow colour aqueous solution of 1mM 4–NP was placed. In the same cuvette, 100 mM 1 ml of $NaBH_4$ solution was added. The mixture of the above solution was stirred for the uniform mixing of 4-NP and $NaBH_4$. The addition of $NaBH_4$ solution results in a transition of the solution's colour. The colour of the mixture gradually darkened which was resulted in to the dark yellow colour. This transformation in colour is attributed to the creation of the nitrophenolate ion [59].

10.57647/ijc.2026.1601.07

In the above solution of 4 -NP and $NaBH_4$, 0.5 ml of monometallic Ag, Ni, and various compositions of bimetallic Ag-Ni catalyst(catalyst concentration: 1 mg/mL, i.e., 0.5 mg catalyst per reaction) was added, which will initiate the reduction reaction. The solutions were continuously stirred for uniform mixing at room temperature using a magnetic stirrer. As the reaction proceeds, there is a change in the concentration of the reactant and product, which will be determined by recording the UV-Visible spectra in the 200–1100 nm range at regular intervals of time. The transformation in the solution's colour also indicates the progress of the reaction. As the reaction proceeds, the concentration of 4-AP increased, which takes place by the evolution of H_2 gas, and the intense yellow colour of the reaction mixture starts fading.

At last, the solution completely turning colourless indicates completion of the reaction, and only the solution completely turns colourless, indicating completion of the reaction and the presence of 4-AP in the solution. [1, 60]. While studying the progress of reaction through UV-Visible spectra, the intensity of the peak at 400 nm starts decreasing, indicating the decrease in the concentration of 4-NP in the reaction mixture as the reaction progresses. Simultaneously, the intensity of the peak at 300 nm increases, indicating an increase in the concentration of 4-AP in the mixture. After the completion of reaction formula given in Eq. number (1) was used to calculate the transformation of 4-NP to 4-AP [8]. In this case, C_0 represents the starting concentration of 4-NP (mg/L), C_t represents the concentration of 4-NP in the reaction mixture (mg/L) at various periods (t), A_t represents the absorbance at time t, and A_0 represents the absorbance at time t = 0 [61].

The catalytic efficiency of the above-synthesized nanoparticles for the degradation of crystal violet dye was examined, along with different contact times, which varied from 0min to 210.0 min in intervals of 30 min [62]. According to the methods outlined, photodegradation of the crystal violet dye took place on the surface of added bimetallic and monometallic nanoparticles of Ag and Ni in the crystal violet dye solution, and it is carried out in the presence of direct sunlight [63].

The adsorption desorption equilibria between the above synthesized nanoparticles and crystal violet dye were enhanced by the thorough mixing through agitation, 50 ml of CV (10 ppm) dye solution was combined with 5 ml of the aforementioned synthesized nanoparticles (catalyst concentration: 1 mg/mL, i.e., 0.5 mg catalyst per reaction).

The above mixture of CV dye and synthesized nanoparticles was then kept in the dark for a time interval of 30 minutes.

The resultant was then exposed to sunlight for 180 minutes, and three millilitres of an aliquot from the reaction mixture were taken out every 30 minutes to track the solution's decrease in absorbance. The mixture of dye and nanoparticles is placed in a 100 ml glass beaker, and it is stirred at 70 rpm on a magnetic stirrer. Additionally, this experiment was carried out in the daytime under direct sunlight between 12:00 noon and 3:00 PM on 20 February 2025 at 35 ± 20 °C. The same conditions were maintained for each set of experiments.

The characteristics peak at λ_{max}= 599 nm show a progressive decrease in intensity, which indicates that the crystal violet dye is degrading. Equation number (2) was used to calculate the percentage of dye degradation (2)[64].The experimental design included explicit controls to distinguish photocatalytic from photolytic degradation: a dark pre-incubation (30 minutes) measured adsorption without photons, while a photolysis control (Table 3, Row 6) showing only 6.25% CV degradation under identical sunlight conditions compared to 62-66% with Ag-Ni catalyst provides definitive proof of 10-fold photocatalytic enhancement over spontaneous photochemical degradation. Solar irradiance was estimated at 800 ± 100 W m^{-2} from Mumbai's February meteorological data (direct beam 600-700 W m^{-2} plus diffuse radiation, latitude 19°N), validated by a maintained reaction temperature of 35 ± 2°C correlating directly with solar heating rates.

Pseudo-first-order kinetic analysis yielded excellent linear fits (R^2 = 0.97-0.99, Fig.s 15-16) throughout the 180-minute reactions, confirming reproducibility with ±3-7% experimental precision and validating the pseudo-first-order kinetic model.

$$\%\ \text{degradation of CV dye or nitrophenol reduction} = ((C_0 - C_t)/C_0) * 100 = ((A_0 - A_t)/A_0) * 100 \quad (1)$$

All experiments were performed in triplicate, and error bars representing standard deviation are shown in the Fig.s. The reproducibility was confirmed by calculating relative standard deviation (%RSD), which was less than 5% for all measurements.

2.6. Antibacterial Activity

The antibacterial activity evaluation of Ag_{100}, Ni_{100}, $Ag_{25}Ni_{75}$, $Ag_{50}Ni_{50}$, and $Ag_{75}Ni_{25}$ was conducted using Gram-positive bacteria, *Bacillus subtilis* QST713 *(B. subtilis)*, *Salmonella typhi* CT18 (S. typhi), *Pseudomonas aeruginosa* ATCC25922 *(P. aeruginosa)*, and Gram-negative bacteria, *Escherichia coli* ATCC12228 *(E. coli)*, *Salmonella typhi* CT18 *(S. typhi)*.

The nutritive medium was infused with bacteria, which were then uniformly dispersed. In each nutrient agar plate, six sterile discs (d = 7 mm) was prepared. Each disc contains 20µl of Ag_{100}, Ni_{100}, $Ag_{25}Ni_{75}$, $Ag_{50}Ni_{50}$, and $Ag_{75}Ni_{25}$ NPs solution, sterile water as a blank (negative control).

10.57647/ijc.2026.1601.07

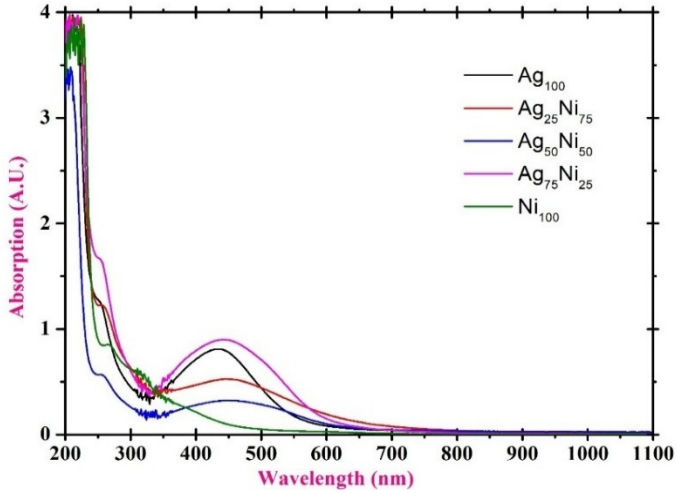

Figure 2. UV-visible analysis of nanocatalyst (a) Ag_{100} (b) $Ag_{25}Ni_{75}$ (c) $Ag_{50}Ni_{50}$ (d) $Ag_{75}Ni_{25}$ (e) Ni_{100}

There is a single standard disc of chloremphenicol, and a single standard disc of chloramphenicol is placed. Then all the agar plates were placed in an incubator whose temperature is 37°C for 24 hours, The zone of inhibition indicate the bactericidal activity of the nanoparticles [65].

3. Result and Discussion

3.1. UV–vis spectrophotometric analysis

The biologically synthesized Ag_{100}, Ni_{100}, $Ag_{25}Ni_{75}$, $Ag_{50}Ni_{50}$, and $Ag_{75}Ni_{25}$ nanoparticles' UV-visible absorption spectra in the 200–1100 nm range are shown in Fig. 2. The absorption band for Ag_{100} at 436 nm indicates the Ag nanoparticle formation, the Ni_{100} centring at 265 nm gives evidence for Ni nanoparticle formation [66, 67]. Similarly, for $Ag_{25}Ni_{75}$, $Ag_{50}Ni_{50}$, and $Ag_{75}Ni_{25}$, the two bands are seen.

The first prominent band obtained at 449 nm, 451nm, 446 nm, and the second band centring at 258nm, 255nm, 255nm for $Ag_{25}Ni_{75}$, $Ag_{50}Ni_{50}$, $Ag_{75}Ni_{25}$. This observation is attributed to the emergence of the Ag-Ni alloy structure [68, 69]. As the concentration of Ni increases, the size of nanoparticles will also increase, and this will eventually decrease peak intensity, and a red shift is also observed [65].

3.1.1. *Optical Properties and Bandgap Analysis*

The optical properties of synthesized monometallic and bimetallic nanoparticles, characterized through UV-Visible absorption spectroscopy, directly demonstrate light-harvesting capability essential for photocatalytic applications. The sharp, intense surface plasmon resonance (SPR) peaks observed at 436 nm for Ag_{100} and 446-451 nm for bimetallic compositions provide evidence of strong visible-light absorption. The red-shift in SPR peak from 436 nm (Ag_{100}) to 449-451 nm (bimetallic samples) indicates composition-dependent modification of electronic structure and enhanced light-matter interaction [70]. Bandgap Energy Estimation: The bandgap energy of synthesized nanoparticles can be estimated from the absorption edge wavelengths observed in UV-Vis spectra using the fundamental relationship $Eg(eV) = 1240/\lambda(nm)$. The absorption edges for monometallic silver appear at approximately 315 nm, corresponding to an estimated bandgap of 3.93 eV. In contrast, bimetallic compositions exhibit absorption edges at longer wavelengths (380-385 nm), corresponding to estimated band gaps of 3.22-3.26 eV for $Ag_{25}Ni_{75}$ and $Ag_{50}Ni_{50}$, and 3.24 eV for $Ag_{75}Ni_{25}$. This reduction in bandgap energy from 3.9 eV (monometallic Ag) to 3.2-3.3 eV (bimetallic)** is a critical finding explaining the superior photocatalytic activity. A reduced bandgap facilitates photon absorption across the visible spectrum (wavelengths up to 400 nm) and reduces the energy requirement for photoinduced electron-hole pair generation, aligning with solar spectrum intensity (peak at ~500 nm). Physical Origin of Reduced Bandgap: The bandgap reduction in bimetallic Ag-Ni nanoparticles arises from the formation of a Schottky barrier at the Ag-Ni interface due to the work function difference (WF_Ni - WF_Ag ≈ 0.85 eV). This interface barrier creates an internal electric field that modulates the electronic band structure, reducing the effective bandgap and enabling stronger solar-light photon absorption. The presence of dual optical absorption features Ag SPR (436-451 nm) and Ni d-d transitions (265 nm) confirms the bimetallic nature and demonstrates complementary light-harvesting across the ultraviolet and visible spectrum [71, 72].

3.2. Fourier transform infrared spectroscopy (FT-IR) analysis

The FTIR spectrum of pure sprout water extract (Fig. 3a) displays characteristic peaks at 3400 cm^{-1} (O-H stretching

10.57647/ijc.2026.1601.07

from polyphenols and flavonoids), 2920 cm^{-1} (C-H stretching from organic compounds), 2100 cm^{-1} (C≡C or C≡N stretching from alkaloids and nitrile-containing compounds), 1640 cm^{-1} (C=O stretching from proteins and carbonyl compounds), and peaks in the region 1000-1500 cm^{-1} corresponding to C-O and C-N stretching vibrations.

These functional groups present in chickpea sprout water are responsible for the reduction and stabilization of metal ions during nanoparticle synthesis. The analysis of FTIR furnishes the information regarding the chemical composition and the functional group present at the surface of nanoparticles through the band obtained in the specific region of the IR spectra. The three main peaks are observed in the IR spectra of Ag, $Ag_{25}Ni_{75}$, and Ni nanoparticles, which are obtained from Fig. 3b-d.

The polyphenolic compounds in sprout water extract contain alcohols and phenols, which is proved by the peaks obtained at 3346.43 cm-1, 3328.5 cm-1,3326.94 cm-1, indicating the occurrence of the O-H group. These compounds will act as a capping agent for nanoparticles. The presence of a carbonyl group is further assisted by the bands seen at wavenumbers 1636.04 cm^{-1} ,1636.40 cm^{-1}, and 1635.56 cm^{-1}. The carbon - carbon, carbon- nitrogen triple bond stretching give rise to the band at 2100.85 cm^{-1}, 2119.96 cm^{-1}, 2109.76 cm^{-1}.

The FTIR spectra of synthesized Ag, $Ag_{25}Ni_{75}$, and Ni nanoparticles (Fig. 3b-d) show retention of characteristic peaks from the sprout extract, confirming the presence of biomolecules as capping agents. The peaks at 3346-3328 cm^{-1} indicate O-H groups from polyphenolic compounds acting as stabilizers. The bands at 2100-2119 cm^{-1}, corresponding to C≡C or C≡N triple bond stretching (originally present in sprout extract), confirm the adsorption of organic phytochemicals on nanoparticle surfaces. The carbonyl peak at ~1636 cm^{-1} further supports the presence of protein and flavonoid molecules as capping agents.

3.3. Morphological Study NTA, EDX analysis, TEM analysis

High resolution transmission electron microscopy was used to further analyze the size, shape, and crystal structure of biosynthesized Ag_{100}, $Ag_{25}Ni_{75}$, and Ni_{100} (HR-TEM). Broad size distribution of Ag_{100}, $Ag_{25}Ni_{75}$, Ni_{100} particles range between 10-40, 10-90, 6-20 nm with mean size of 23.73±6.42, 44.72±18.80, 12.96±3.66 nm as depicted in Fig. 5a, Fig. 5b, and Fig. 5c. The shape of Ag particles is not perfectly spherical, and it is well distributed, whereas the $Ag_{25}Ni_{75}$ particles are pseudocubic with little aggregation of nuclei, and also depicted alloy structure as observed in Fig. 4a and Fig. 4b. The particles of Ni are perfectly spherical in shape as observed in Fig. 4c. Fig. 6 illustrate the Selected Area Electron Diffraction (SAED) pattern of Ag_{100}, $Ag_{25}Ni_{75}$,Ni_{100} express polycrystalline nature and FCC structure, with that lattice planes (111), (200), (220), and (311) clearly listed which will be in accordance with the XRD data [68, 73–75].

The core-shell architecture of Ag-Ni bimetallic nanoparticles is confirmed through comprehensive analysis of SAED patterns and TEM imaging. The SAED pattern of $Ag_{25}Ni_{75}$ illustrated in Fig. 6b displays well-defined polycrystalline diffraction rings with distinctly sharp, intense bright spots characteristic of crystalline phases, which is typical of core-shell structures rather than the diffuse, broadened rings observed in random alloy nanoparticles. Furthermore, the sequential reduction based on reduction potential differences (Ag^{+}/Ag^{0} = +0.799 V vs. Ni^{2+}/Ni^{0} = -0.257 V) ensures that silver reduces first to form the core, followed by nickel shell deposition. The HR-TEM images showing pseudocubic morphology with interface features further corroborate the core-shell configuration rather than a homogeneous alloy structure.

Fig. 8, reveals the elemental composition of monometallic Ag, Ni and $Ag_{25}Ni_{75}$ bimetallic nanoparticles. In EDX spectra of monometallic Ag and Ni the peaks for only Ag and Ni can be seen at around 3 Kev and 7.5 Kev with weight % 62.14 and 13.95 whereas for bimetallic $Ag_{25}Ni_{75}$ the peaks for both Ag and Ni obtained at around 3 Kev and 7.5 Kev with weight % 25.04 and 5.53. The signal for oxygen and signal other than Ag and Ni could be because of constituent element of sprout water extract. The synthesis of monometallic and bimetallic nanoparticles of Ag and Ni was confirmed by this result.

The hydrodynamic diameters obtained from NTA (21-42 nm) are consistently larger than those measured by TEM (10-90 nm), which is expected due to fundamental differences in measurement principles. NTA measures the effective diameter of particles moving under Brownian motion in aqueous medium, which includes the solid metal core plus the hydration layer, surface-adsorbed phytochemicals from the sprout water extract, and potential particle agglomeration. In contrast, TEM measures on

ly the solid metal core in dry, vacuum conditions. The hydrodynamic diameter being 1.5-2× larger than the physical diameter is well-documented for biologically synthesized nanoparticles and validates the presence of organic stabilizers on the nanoparticle surface, which is essential for colloidal stability. This size difference confirms successful green synthesis with phytochemical capping agents. In addition to the primary elements Ag and Ni, the EDX spectra (Fig. 8) display signals for oxygen (O), carbon (C), and trace amounts of other elements such as sulfur (S), phosphorus (P), potassium (K), and calcium (Ca).

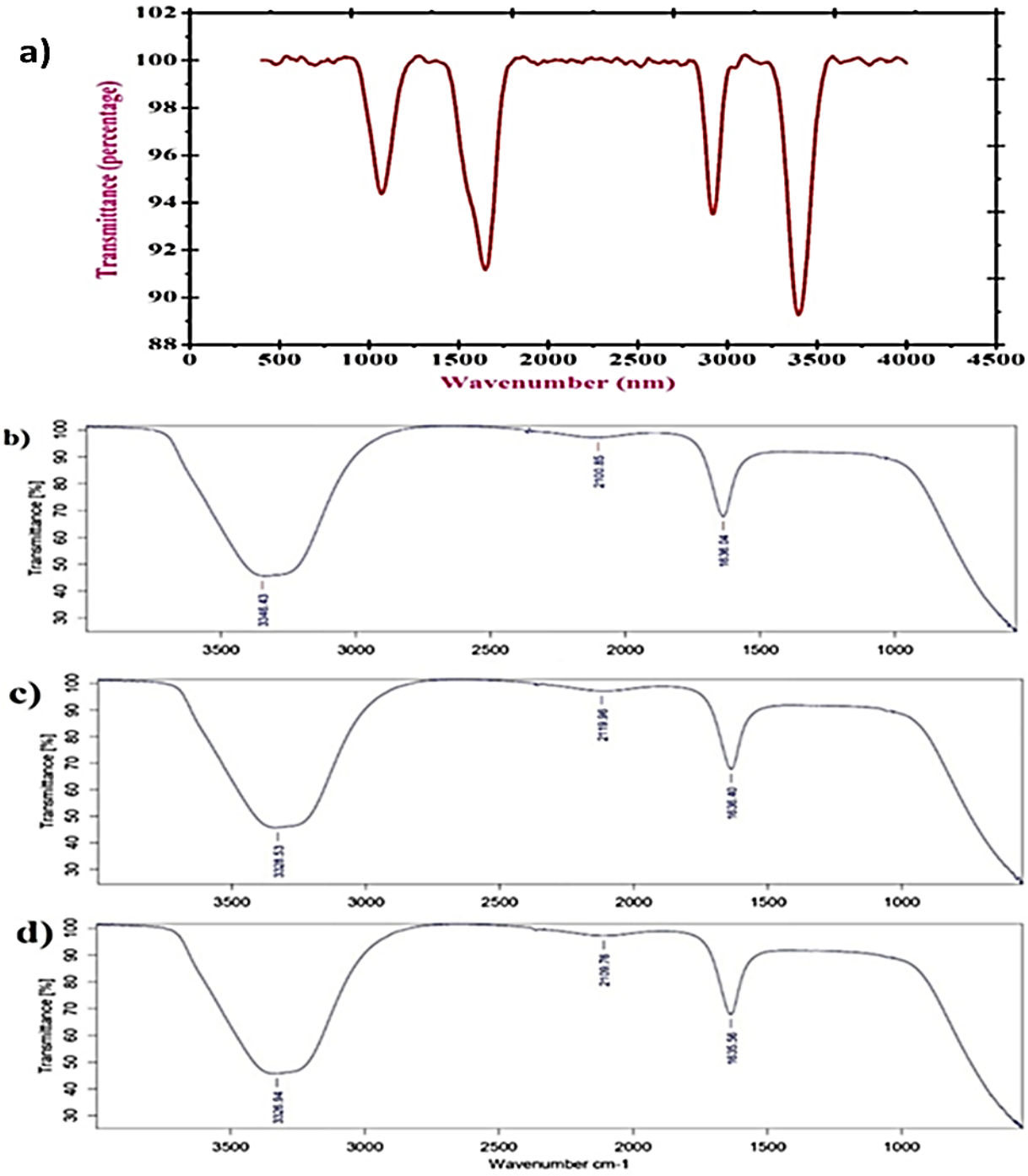

Figure 3. FT-IR spectrum of nanocatalyst (a) sprout water (b) Ag_{100} (c) $Ag_{25}Ni_{75}$ (d) Ni_{100}

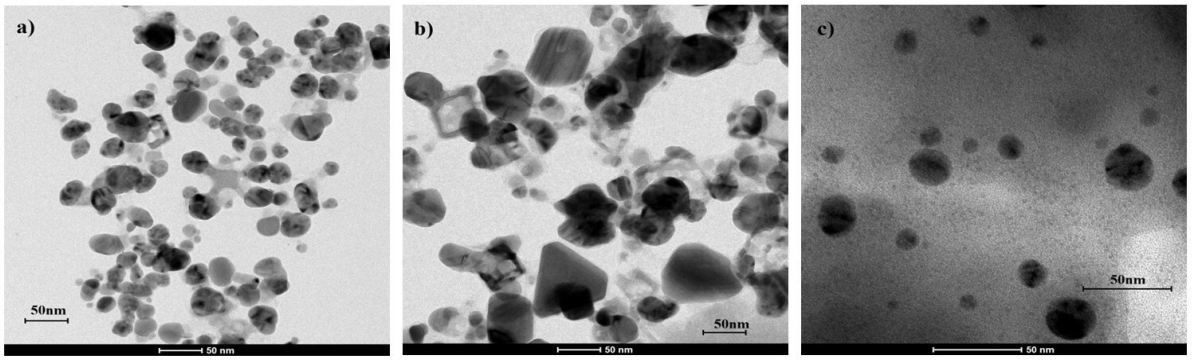

Figure 4. HR-TEM images of nanocatalyst (a) Ag_{100} (b) $Ag_{25}Ni_{75}$ (c) Ni_{100}

10.57647/ijc.2026.1601.07

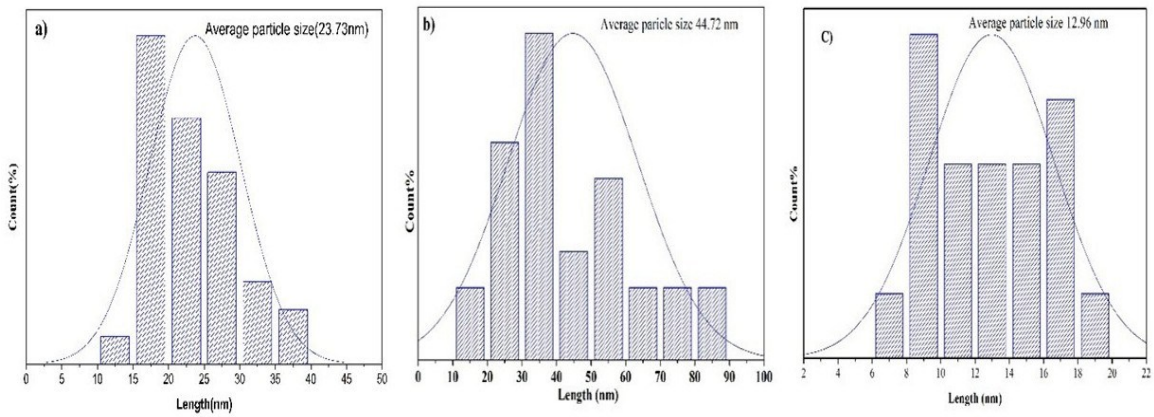

Figure 5. Histogram of nanocatalyst (a) Ag_{100} (b) $Ag_{25}Ni_{75}$ (c) Ni_{100} catalyst

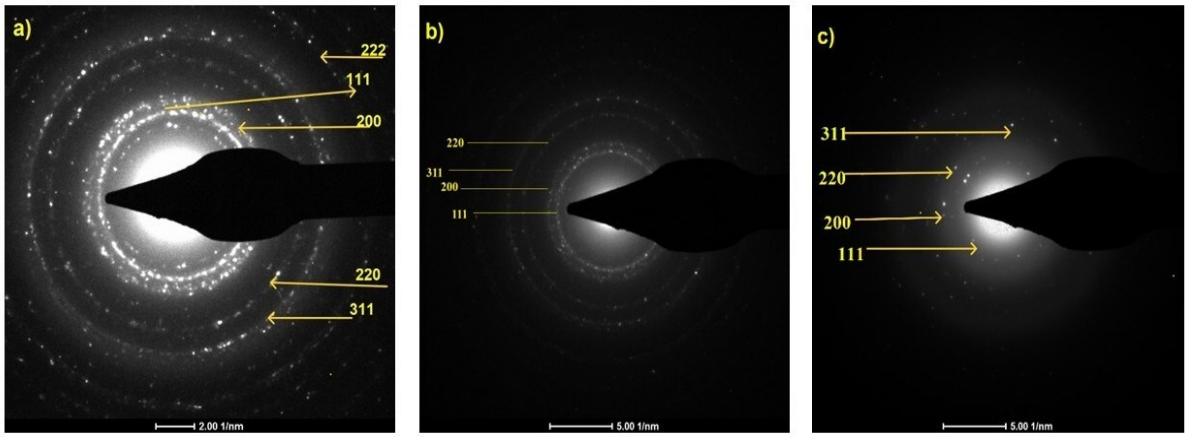

Figure 6. SAED pattern of nanocatalyst (a) Ag_{100} (b) $Ag_{25}Ni_{75}$ (c) Ni_{100}

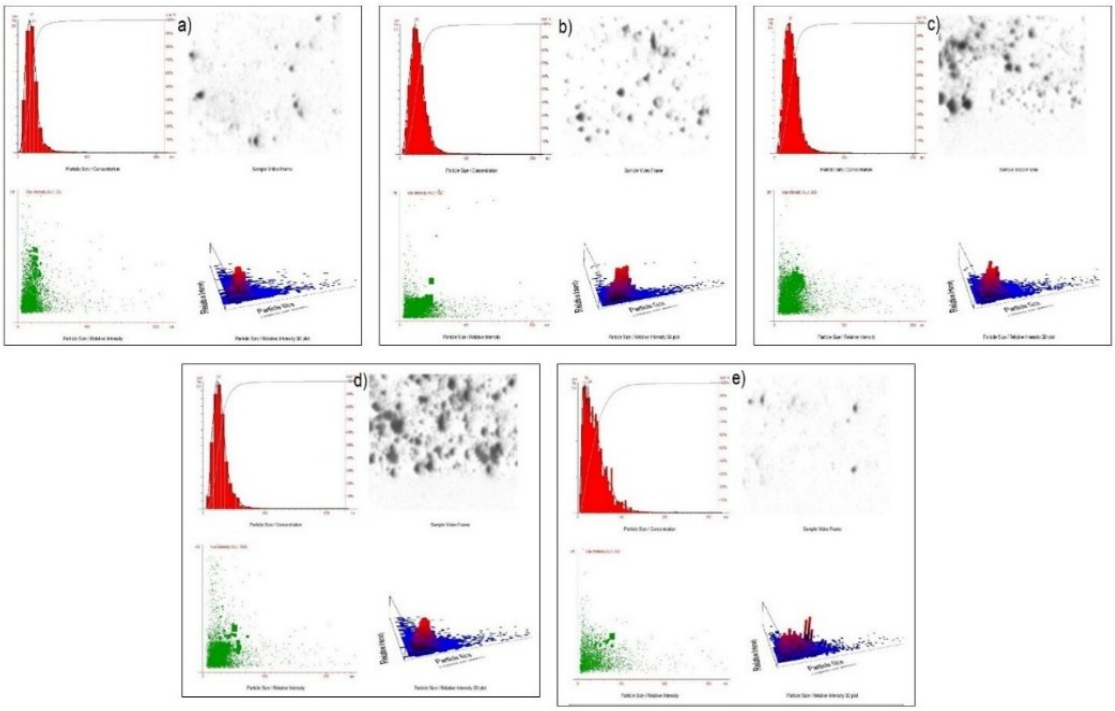

Figure 7. NTA analysis of nanocatalyst (a) Ag_{100} (b) $Ag_{25}Ni_{75}$ (c) $Ag_{50}Ni_{50}$ (d) $Ag_{75}Ni_{25}$ (e) Ni_{100}

NTA analysis of biosynthesized Ag, $Ag_{25}Ni_{75}$, $Ag_{50}Ni_{50,}$ $Ag_{75}Ni_{25,}$ Ni nanoparticles discloses the mean size of nanoparticles was 21 nm, 29 nm, 26 nm, 30 nm, 42nm which is observed in Fig. 7a, Fig.. 7b, Fig.. 7c, Fig.. 7d, Fig..7e. The standard deviation of above naopatricle was 12 nm, 19 nm, 17 nm, 17 nm, 34 nm respectively.

10.57647/ijc.2026.1601.07

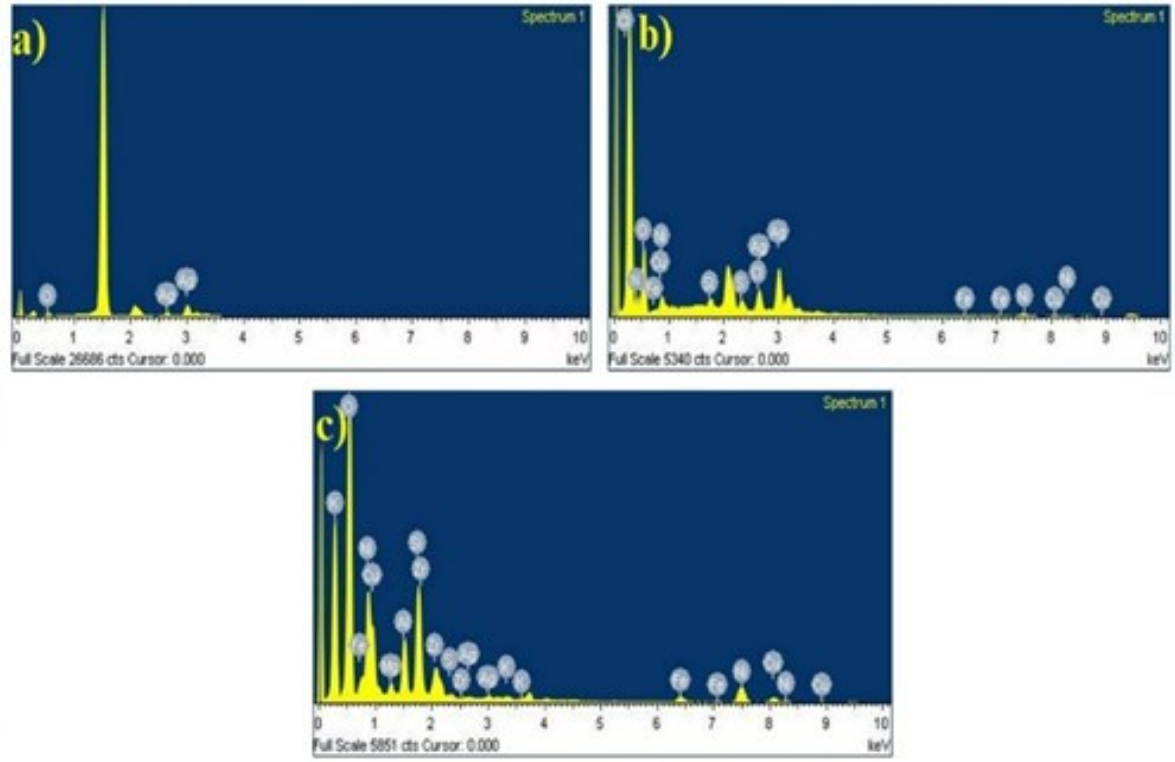

Figure 8. EDX spectra of nanocatalyst (a) Ag_{100} (b) $Ag_{25}Ni_{75}$ (c) Ni_{100}

These additional elements originate from the phytochemical constituents of chickpea sprout water extract used as reducing and capping agents. Origin of additional elements:

- Oxygen and Carbon: Main components of polyphenolic compounds, flavonoids, proteins, and carbohydrates that act as capping agents on nanoparticle surfaces

- Sulfur: From sulfur-containing amino acids (cysteine, methionine) in proteins present in sprout extract:

- Phosphorus: From phospholipids, nucleotides, and phosphorylated proteins

- Potassium and Calcium: Mineral nutrients naturally present in chickpea sprouts. These biomolecules adsorb on nanoparticle surfaces during synthesis and remain as an organic corona even after washing, contributing to colloidal stability and preventing aggregation. The presence of these elements confirms successful green synthesis with biological capping agents, which is a characteristic feature distinguishing biologically synthesized nanoparticles from chemically synthesized ones. The organic corona does not interfere with catalytic activity; rather, it enhances stability and dispersibility in aqueous medium, which is beneficial for environmental applications.

3.4. XRD analysis

The data obtained from XRD analysis was used to investigate the phase purity and composition of Ni@Ag nanostructures across different mass ratios. Fig. 9. displayed diffraction pattern of synthesized Ag, Ni, $Ag_{25}Ni_{75}$, $Ag_{50}Ni_{50}$, $Ag_{75}Ni_{25}$. The diffraction pattern of all the samples clearly revealed the FCC structure. In the XRD spectra, diffraction peaks were obtained at 2θ = 27.8^0, 32.2^0, 38.1^0, 44.2^0, 46.2^0, 54.8^0, 57.4^0, 64.4^0,77.01^0. The value of diffraction indicates the crystal plane (210), (122), (111), (200), (231), (142), (241), (220), and (311). These values of crystal planes give the structure of face-centred cubic (FCC) Ag. This value completely coincides with the value given by the Joint Committee on Powder Diffraction Standards (JCPDS card no 04-0783. Monometallic nickel nanoparticles were subjected to powder XRD analysis using a Rigaku MiniFlex 300/600 diffractometer equipped with an advanced D/teX Ultra detector system. The measurement employed Cu Kα radiation (λ = 0.15406 nm) at 40 kV and 15 mA, with optimized parameters: scan speed 4.00°/min, step width 0.02°, and continuous θ/2θ geometry over a 2θ range from 3° to 80°. The XRD analysis of nickel nanoparticles yielded thirteen clearly resolved, well-defined diffraction peaks with excellent peak sharpness (full-width at half-maximum, FWHM: 0.04°-0.50°) and strong base peak intensity of 3425 counts per second, indicating high-quality data with a superior signal-to-noise ratio (>100). The three major characteristic peaks appeared at 2θ = 41.970°(±0.013°), 47.189°(±0.007°), and 51.7°(±0.5°), unambiguously assigned to Miller indices (111), (220), and (200) planes, respectively, of face-centered cubic (FCC) nickel structure. These experimental peak positions precisely matched literature values from the

JCPDS card number. 04-0850, confirming phase purity and crystalline structure. The successful identification of multiple higher-order diffraction planes ((111), (200), (220), etc.) demonstrates the excellent angular resolution capability of the instrumental setup, which is not achievable with low-quality diffractometry equipment. The identification of 13 distinct peaks (compared to typically 3-5 for poorly crystalline materials) further substantiates the high crystallinity and quality of the synthesized nickel nanoparticles.In all the composition of Ni@Ag, ten different diffraction peaks are observed: 27.8^0, 32.2^0,38.1^0, 44.2^0, 46.2^0, 54.8^0, 57.4^0, 64.4^0, 76.6^0, 77.3^0. The Debye Scherrer formula $D = \frac{K\lambda}{\beta\, cos\theta}$ is employed to compute the average crystal size of the above synthesized nanoparticles Where β is the angular FWHM (full-width at half maximum) of the XRD peak at the diffraction angle θ, D is the average crystalline size of the nanoparticles, while K is geometric factor (0.9) and λ signifies the wavelength of X-ray radiation source [66]. The calculated average crystallite size of Ag, $Ag_{25}Ni_{75}$, $Ag_{50}Ni_{50}$, $Ag_{25}Ni_{75}$, and Ni nanoparticles are 16.56 nm, 73.53 nm, 66.80 nm, 46.27 nm, and 60.14 nm. The calculated average crystallite size for monometallic nickel (Ni_{100}) was 60.14nm, which shows excellent consistency with transmission electron microscopy observations (6-20 nm core diameter with ~40-60 nm total particle size including organic capping layer) and SAED pattern analysis confirming polycrystalline FCC structure. This agreement between XRD-derived and TEM-measured particle sizes validates the reliability of both characterization techniques and demonstrates the quality of the XRD data acquisition and analysis.

3.4.1. Evidence for Core-Shell Architecture from XRD and SAED

XRD analysis shows peaks corresponding to both FCC Ag and Ni phases, the interpretation requires careful consideration of core-shell nanostructure characteristics. For bimetallic core-shell nanoparticles where both metals possess FCC crystal structure with similar lattice parameters (Ag: 4.086 Å, Ni: 3.524 Å), the diffraction peaks naturally appear overlapped rather than showing distinct separate peaks. This is fundamentally different from a true solid-solution alloy, which would exhibit peak positions intermediate between the two pure metals with systematic shifts based on composition.

Our XRD patterns (Fig. 9) display peaks at 2θ positions corresponding to both pure Ag (JCPDS 04-0783) and pure Ni (JCPDS 04-0850) reference patterns, without intermediate peak positions characteristic of alloy formation. This observation, combined with the SAED evidence, supports a core-shell architecture rather than an alloy structure.

The SAED pattern analysis provides definitive evidence for a core-shell configuration. The SAED pattern of $Ag_{25}Ni_{75}$ (Fig. 6b) exhibits well-defined polycrystalline diffraction rings with distinctly sharp, intense bright spots characteristic of crystalline phases.

This pattern is typical of core-shell structures, where each component maintains its individual crystal structure, in contrast to the diffuse, broadened rings observed in random alloy nanoparticles, where lattice strain and compositional gradients create disorder.

Furthermore, the compositional analysis by EDX showing varying Ag: Ni ratios at different measurement points supports the core-shell model. In a homogeneous alloy, EDX analysis would yield consistent composition throughout the sample.

The observed compositional heterogeneity is consistent with the proposed Ni-core@Ag-shell architecture, where EDX spot analysis on different nanoparticle regions yields varying Ag: Ni ratios depending on whether the electron beam probes the Ni-rich core or the Ag-enriched shell regions.

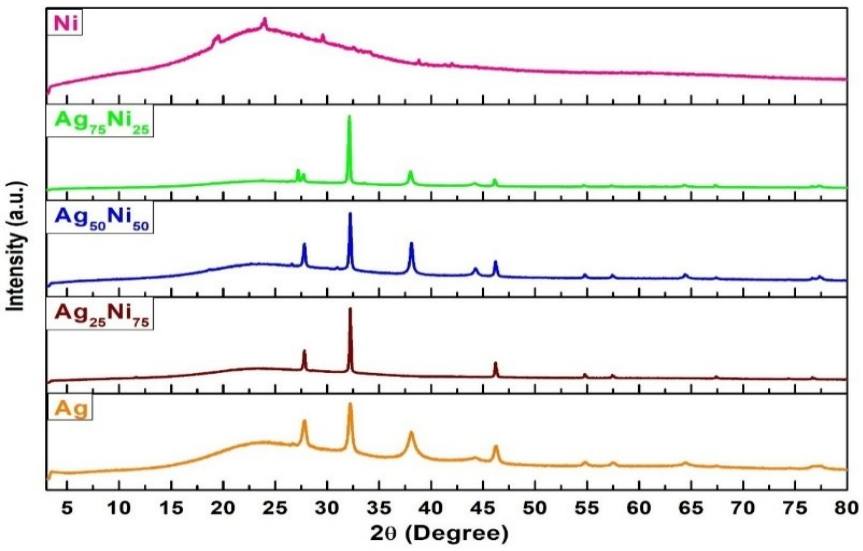

Figure 9. XRD diffraction pattern of (a) Ag_{100} (b) $Ag_{25}Ni_{75}$ (c) $Ag_{50}Ni_{50}$ (d) $Ag_{75}Ni_{25}$ (e) Ni_{100} catalyst

10.57647/ijc.2026.1601.07

3.5. Mechanism of core-shell Ag-Ni nanoparticles formation

The process of reduction of metal ions will result in the formation of metallic core-shell nanoparticles. It is possible via two method seed -growth and seedless. In the seed growth method, the metal that takes the position of the core is reduced first due to its higher reduction potential, and the metal that acts as the shell is developed on it. In the seedless approach, metal precursors are combined with agents that serve dual roles as reducers and stabilizers. The sprout water extract serves as a dual-purpose agent, acting both as a reducer and stabilizer, in a one-step, seedless approach to create Ag-Ni bimetallic core-shell nanoparticles. In this method, reduction of metal ions will take place according to their reduction potential[60]. In the solution of silver nitrate and nickel nitrate hexahydrate, the silver metal has a higher reduction potential; thus, Ag will reduce first (Ag+/Ag0 = 0.799 V) and will take the position of core. The reduction of Nickel will take place on the surface of Ag core as it possesses lower reduction lower reduction (Ni^{+2}/ Ni^0 = 0.257 V) and served as shell. The coordinating nature of reducing agent also play vital role in co-reduction process for formation of core shell structure [59]. The key problem in seedless method is reduction of two metal with different reduction potential and regulating nucleation. Nanoparticle nucleation and growth are influenced by the reducing agent and surface ligands. The metal which possesses high reduction potential will reduces and create nucleation site which will further help in development of nanoshell. Reverse core shell structures are achievable when a surface ligand binds to a metal that possesses a higher reduction potential, provided that the structure maintains its stability [76]. The rate of reduction of Ag^+ to Ag^0 is faster than Ni^{+2} to Ni^0 which will result in to the Ag_{core} followed by Ni_{shell}. The phytochemical present in the sprout water extract like polyphenols and flavonoids reduced first Ag^+ then it is followed by reduction of Ni^{+2} which will occurred on the Ag^0seed surface based on their reduction potential value [77]. The sequential reduction based on reduction potentials (Ag^+/Ag: 0.799 V, Ni^{2+}/Ni: -0.257 V) ensures formation of core-shell structure, a feature not previously reported for Ag-Ni synthesis using plant-based reducing agents.

3.5.1. *Thermodynamic Feasibility of Green Reduction*

The reduction of Ag^+ and Ni^{2+} to their metallic states is thermodynamically favorable when considering the reduction potentials:

Metal reduction potentials:

$Ag^+ + e^- \rightarrow Ag^0$; E° = +0.799 V

$Ni^{2+} + 2e^- \rightarrow Ni^0$; E° = -0.257 V

Reducing agents in sprout water extract:

Polyphenolic compounds (such as flavonoids, phenolic acids) act as reducing agents:

General reaction: Polyphenol-(OH) → Polyphenol-O + H^+ + e^-

Typical oxidation potential of polyphenols: E° = +0.5 to +0.8 V (vs. SHE)

Thermodynamic analysis:

For Ag^+ reduction:

E°cell = E°(Ag^+/Ag^0) - E°(polyphenol oxidation) = 0.799 - 0.6 ≈ +0.2 V

ΔG° = -nFE° = negative (thermodynamically favorable)

For Ni^{2+} reduction:

E°cell = E°(Ni^{2+}/Ni^0) - E°(polyphenol oxidation) = -0.257 - 0.6 ≈ -0.86 V

ΔG° = -nFE° = positive (thermodynamically unfavorable under standard conditions)

However, Ni^{2+} reduction becomes feasible due to:

1. Complexation effect: Polyphenols complex with Ni^{2+}, shifting the reduction potential to more positive values

2. pH effect: The synthesis is conducted at pH ~8-9 (basic conditions from NH_3 released during sprouting), which shifts Ni^{2+}/Ni^0 potential more positive

3. Surface catalysis: Once Ag^0 nuclei form, they catalyze the reduction of Ni^{2+} through galvanic reduction

4. Kinetic factors: The synthesis at elevated temperature (60°C) overcomes activation barriers

The higher reduction potential of Ag^+ ensures preferential reduction of silver first, forming nucleation sites. Subsequently, Ni^{2+} reduces on the Ag surface through catalytic electron transfer, resulting in the core-shell architecture.

3.6. Catalytic reduction of 4-nitrophenol and crystal violet dye and its UV -visible analysis discussion

The Absorption peaks for the 4-NP are observed at 316 nm, as mentioned in the graph. The addition of 0.5 ml of $NaBH_4$ results in the peak transitioned from 316 nm to 401 nm, which was attributed to the rise in the solution's pH, leading to the fabrication of the nitrophenolate ion. After 20 minutes, the peak at 410 nm remains constant in the absence of a catalyst. Following the introduction of the catalyst, the peak at 401 nm starts to lose intensity, and simultaneously, a new peak at 302 nm becomes evident in the spectra. As the reaction advances, the intensity of the newly formed peak grows, verifying the production of 4-AP. Fig. 10 illustrates the UV-visible spectroscopy analysis of the 4-NP reduction process, employing catalysts such as Ag, $Ag_{25}Ni_{75}$, $Ag_{50}Ni_{50}$, $Ag_{75}Ni_{25}$, and Ni. The kinetic order for the 4-NP reduction process is pseudo-first order. The calculations of the rate constant (kapp) required the graph of reduction time versus ln(At/A0) to be plotted as seen in Fig. 12. The pseudo-

first-order equation for the reduction of 4-NP is given below.

$$r = lnC_t / C_0 = d_c / d_t = -K_{app}t \quad (1)$$

where r represented the reduction rate; t represented reduction time; while concentration represented by c; C_0 is the concentration of reactants when the reaction starts at time t = 0; Ct is the concentration of reactants after a certain time interval t. The reaction rate can be expressed in terms of comparative absorption intensity as the reaction 4-NP has maximum absorption intensity in visible region therefore the equation of pseudo first order reaction of 4-NP can be expressed in terms of absorption intensity.

$$r = lnC_t / C_0 = lnA_t / A_0 = -K_{app}t \quad (2)$$

The graph of $\ln(A_t/A_0)$ versus time required for the reduction process for each of the five catalysts, Ag, Ag25Ni75, Ag50Ni50, Ag75Ni25, Ni, and their kinetic data are represented in Fig. 11 and Fig. 12. The percentage of 4-NP reduction by monometallic Ag and nickel were 74.18 % in 180 seconds, 80.55% in 240 sec. Similarly, the remaining compositions $Ag_{25}Ni_{75}$, $Ag_{50}Ni_{50}$, and $Ag_{75}Ni_{25}$ show reduction percentages of 84.69% in 60 seconds, 77.82% in 300 seconds, and 50.26% in 240 seconds.

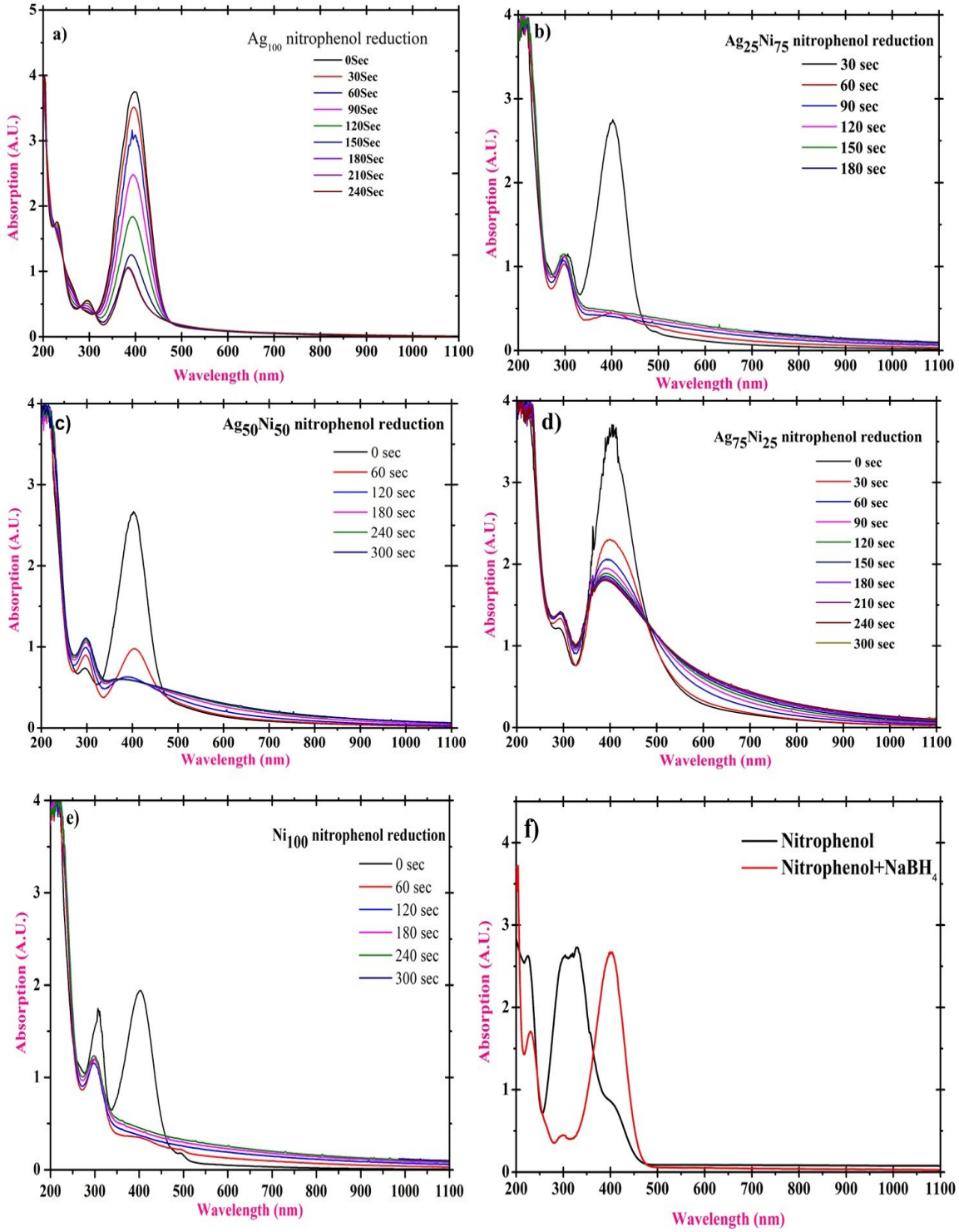

Figure 10. UV-visible study of 4-Nitrophenol reduction by nanocatalyst (a) Ag_{100} (b) $Ag_{25}Ni_{75}$ (c) $Ag_{50}Ni_{50}$ (d) $Ag_{75}Ni_{25}$ (e) Ni_{100} (f) Nitrophenol+$NaBH_4$

10.57647/ijc.2026.1601.07

If we compare the reduction percentage, $Ag_{25}Ni_{75}$ shows maximum degradation within a very short period of time and proves maximum efficiency in the process of reduction of 4-NP. The process of reduction of 4-NP by monometallic Ag and Ni catalyst has a calculated rate constant of 0.0067 sec^{-1} and 0.0045 sec^{-1}. The rate constant for bimetallic $Ag_{25}Ni_{75}$, $Ag_{50}Ni_{50}$, $Ag_{75}Ni_{25}$ are 0.0117 sec^{-1}, 0.0043 sec^{-1}, 0.0022sec^{-1}. The kinetic study of the nitrophenol reduction plot in the presence of a catalyst helps to calculate the value of the rate constant (k) and R^2 as mentioned in Table 2.

The kinetic analysis of 4-nitrophenol reduction was performed using the pseudo-first-order model: $\ln(A_t/A_o) = -kappt$, where A_t is absorbance at time t and A_o is initial absorbance. All calculations were performed using consistent time units (seconds), and the linear plots are shown in Fig. 12.

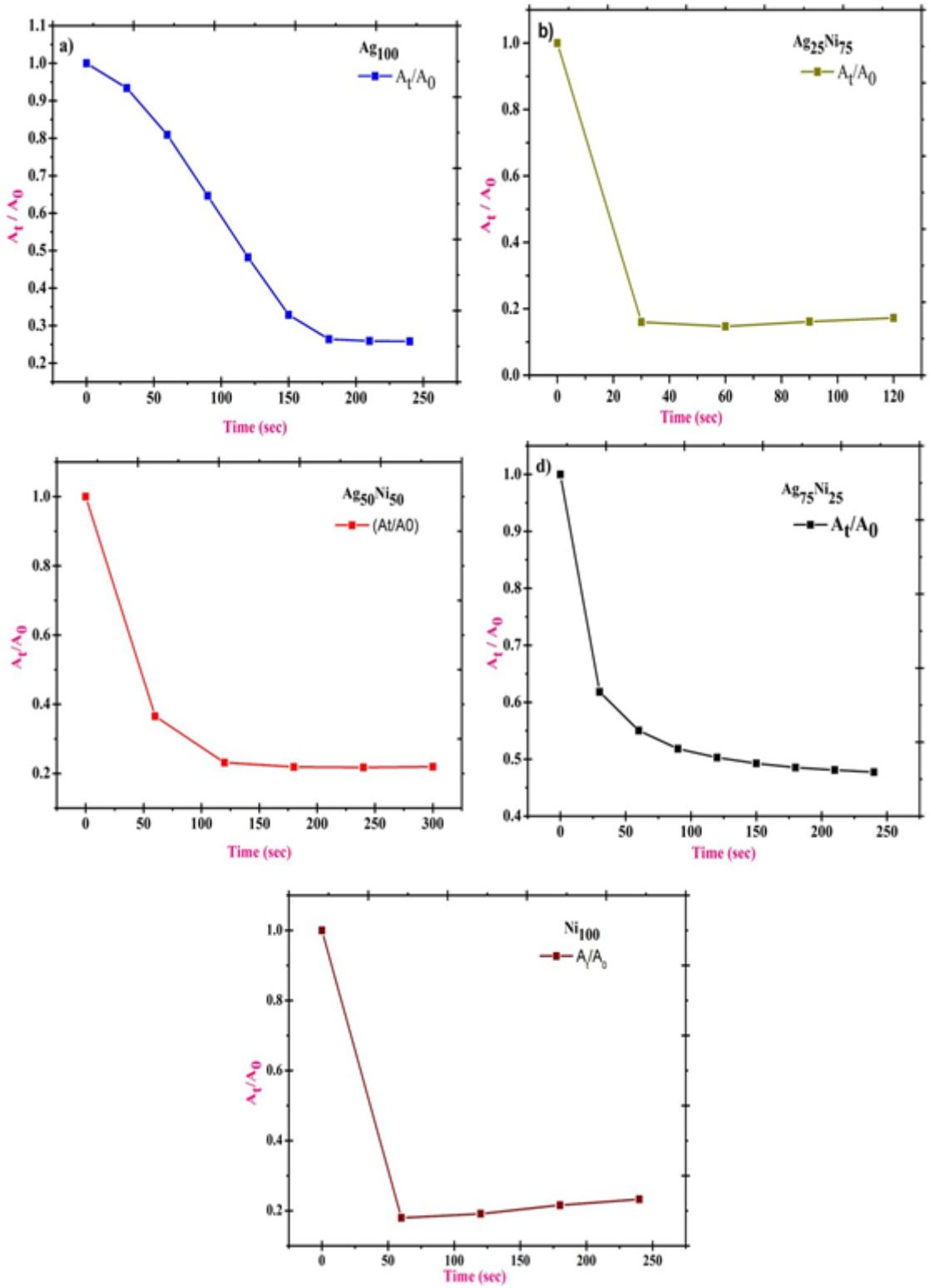

Figure 11. Graph of A_t / A_0 versus reduction time by nanocatalyst (a) Ag_{100} (b) $Ag_{25}Ni_{75}$ (c) $Ag_{50}Ni_{50}$ (d) $Ag_{75}Ni_{25}$ (e) Ni_{100} Error bars represent standard deviation from triplicate measurements (n:3)

10.57647/ijc.2026.1601.07

The correlation coefficients (R^2) vary significantly among different catalysts. Ag_{100} shows an excellent fit to the pseudo-first-order model (R^2 = 0.9403), indicating classical pseudo-first-order kinetics. However, $Ag_{25}Ni_{75}$, despite showing the highest catalytic activity (84.69% degradation in 60 s, k = 0.0117sec^{-1}), exhibits a lower R^2 = 0.2750. This deviation from ideal pseudo-first-order behavior is attributed to the extremely rapid initial reaction kinetics.

When degradation occurs faster than the measurement interval (most degradation is complete within 30 seconds), the system cannot achieve steady-state conditions assumed by pseudo-first-order kinetics. This results in mixed-order or diffusion-limited kinetics during the initial phase, transitioning to pseudo-first-order only after significant substrate depletion. Similar deviations have been reported for highly active catalysts where mass transfer limitations and rapid surface reactions compete. The achieved degradation rate of 84.69% in 60 seconds with a rate constant of 0.0117 sec^{-1} represents one of the fastest reported rates for Ag-Ni bimetallic catalysts in the literature. The rate constants correlate with the synergistic effect observed in bimetallic compositions, with $Ag_{25}Ni_{75}$ showing the highest activity, demonstrating that an appropriate Ag: Ni ratio optimizes electron transfer and catalytic efficiency.

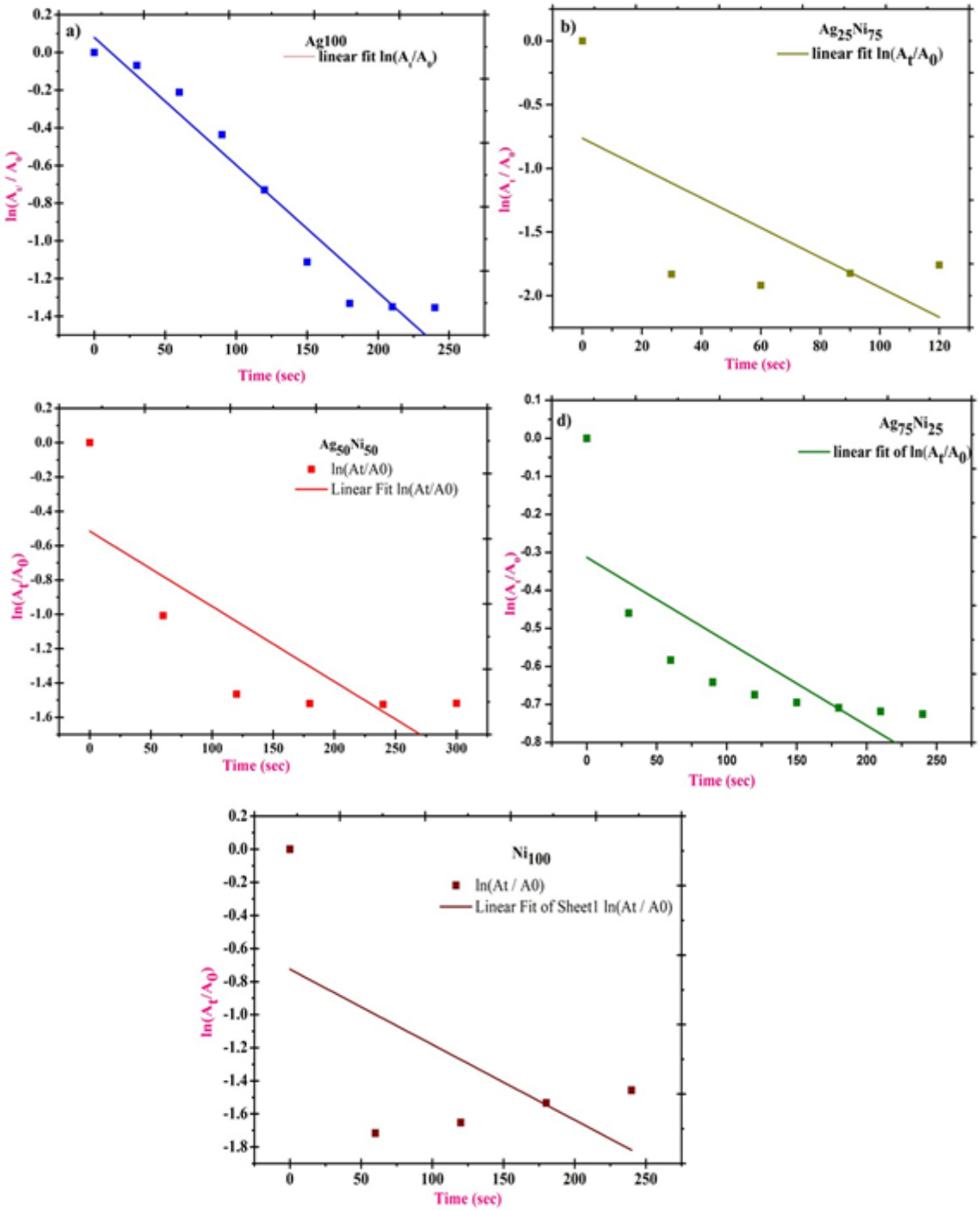

Figure 12. Graph of $\ln(A_t / A_0)$ versus reduction time by nanocatalyst (a) Ag_{100} (b) $Ag_{25}Ni_{75}$ (c) $Ag_{50}Ni_{50}$ (d) $Ag_{75}Ni_{25}$ (e) Ni_{100} Data points are mean values from three independent experiments; error bars show standard deviation

10.57647/ijc.2026.1601.07

Table 2. Percentage of 4-NP reduction, rate constant and R^2 of nanocatalyst (a) Ag_{100} (b) $Ag_{25}Ni_{75}$ (c) $Ag_{50}Ni_{50}$ (d) $Ag_{75}Ni_{25}$ (e) Ni_{100}

Sr.No.	Catalyst (NPs)	% of degradation of 4-NP (seconds)	Rate constant (k)(sec^{-1}) with standard deviation	R^2
a.	Ag_{100}	74.18% in 180 seconds	0.0067±0.0006	0.9403
b.	$Ag_{25}Ni_{75}$	84.69% in 60 seconds	0.0117±0.00737	0.2750
c.	$Ag_{50}Ni_{50}$	77.85% in 300 seconds	0.0043±0.0016	0.5659
d.	$Ag_{75}Ni_{25}$	50.26% in 240 seconds	0.0022±0.0006	0.5533
e.	Ni_{100}	80.55% in 240 seconds	0.0045±0.0034	0.1492

3.6.1. *Mechanism of nitrophenol reduction*

The reducing agent sodium borohydride alone unable to reduce 4-NP completely. Thermodynamically two factors are responsible for the failure of $NaBH_4$ first is due the repulsion between the 4-NP and BH_4^- which possess same charge give rise to electrostatic repulsion and second is due to the potential energy gap between $BH_4^-$and nitro - NO_2group.

The role of borohydride ion as a powerful reducing agent in aqueous phase is possible due to its reduction potential (E for H_3BO_3/BH_4 = - 1.33 V). The process of reducing 4-NP in water is thermodynamically viable (E for 4-NP/4-AP is 0.76 V).

The reaction involving borohydride and the nitrophenolate ion is not favoured from a kinetic perspective[60]. In the process of reduction electron is donated by (BH_4^- ion) and accepted by ($C_6H_5NO_2^-$ion) which is facilitate by the synthesized nanomaterial and this will help to eliminate the kinetic barrier and promote the reduction process of 4-NP. The catalytic reduction process of 4-NP is pseudo first order kinetic and in presence of $NaBH_4$ as reducing agent.

The number of electrons involved in the above reduction reaction is six. The movement of electrons from borohydride to nitrophenolate ion involved the adsorption of both the species on the active site of catalyst surface. The speed of the reduction reaction increased due to the lowering of energy of activation which is done by Ag and Ni acting as effective catalyst.

The reduction reaction of 4-NP is not possible only by sodium borohydride in absence of catalyst which is further proved experimentally. The role of biosynthesized Ag-Ni nanoparticles is to provide strong metal-support and surface for the electron transfer mechanism which enhances the ions migration and speed up the reduction reaction of 4-NP in the presence of BH_4^- ions. The Ag-Ni surface acts as electron deficient species while BH_4^- is negatively charged species adsorbed on Ag-Ni nanocatalyst surface which is deficient of electron[59]. As per Langmuire Hinshelwood mechanism before the reaction both the reactants 4-NP and BH_4^- adsorbed on to the catalyst surface. The generation of active hydrogen atom took place due to the cleavage of B-H bond which is assisted by donation of electron from BH_4^- ion to the electron deficient Ag-Ni nanocatalyst. This will further combine with unreacted hydrogen species of which on the surface of Ag-Ni and resulted in to the production of hydrogen gas [58].

This is confirmed by the bubbles in the reaction mixture which will further proceed the reaction. This easily generated hydrogen species, promotes the conversion of 4-NP to 4-AP which is assisted by it's adsorption and transfer of electron on to the catalyst surface.

This provides Ag-Ni as effective green catalyst for conversion of 4-NP to economically valuable 4-AP. The photocatalytic degradation kinetics were analyzed using the Langmuir-Hinshelwood (L-H) model, which describes the relationship between initial degradation rate and initial concentration of pollutant.

According to the L-H model:

$r = -dC/dt = (kKC)/(1 + KC)$

where r is the degradation rate, k is the rate constant, K is the adsorption equilibrium constant, and C is the concentration.

At low concentrations ($KC << 1$), the equation simplifies to pseudo-first-order:

$r = kKC = kapC$, where $kap = kK$

This concentration-dependent behavior has been extensively documented for various photocatalytic systems, including Zn(II)/Ni(II) magnetic heterostructure ferrite [78]. In our system, the pseudo-first-order behavior observed for CV degradation confirms that the dye concentration (10 ppm) falls in the low-concentration regime where adsorption is not saturated and the reaction rate is linearly proportional to concentration. The rate constants obtained from the L-H model provide insights into both adsorption (K) and surface reaction rate (k) contributions to overall catalytic activity. The higher rate constants for bimetallic compositions suggest enhanced both adsorption and electron transfer efficiency compared to monometallic counterparts. The evaluation of photocatalytic degradation efficiency of the above synthesized monometallic and bimetallic NPs for the organic dye pollutants, crystal violet, under solar radiation is shown in Fig. 13. The photocatalytic activity of monometallic Ag, Ni, and bimetallic $Ag_{25}Ni_{75}$, $Ag_{50}Ni_{50}$, and $Ag_{75}Ni_{25}$ NPs was carried out to find the most efficient catalyst among the prepared samples. The above

10.57647/ijc.2026.1601.07

synthesized samples were subjected to the crystal violet dye degradation using solar light at various time intervals, serving as a reaction model to evaluate its photocatalytic activity. The relative absorption band for crystal violet dye was depicted at 588 nm, which will represent the n goes to pi to the asterisk operator transition, and 302 nm mentioned the benzoic ring structure, respectively [79]. The photocatalysis of 10ppm crystal violet dye solution was carried out in the absence of a catalyst under solar light irradiation. The result showed the decrease in the absorption intensity of the mixture as the time proceeds, which indicates the degradation of the dye, which will vary for each catalyst. The total irradiation time was 3 hrs, which is constant for every catalyst. The degradation efficiencies of solar radiation in the absence of a catalyst were 6.25% which is very low, as shown in Fig. 14a. After the addition of the above synthesized monometallic and bimetallic catalyst of Ag-Ni to the dye solution, the process of adsorption-desorption equilibrium took place, which further enhances the photodegradation of the dye. The time-dependent UV-visible absorption spectra for the degradation of CV dye with the addition of monometallic Ag, Ni, and bimetallic Ag25Ni75, Ag50Ni50, and $Ag_{75}Ni_{25}$ NPs as a catalyst under solar light irradiation for different time intervals are shown in Fig. 14b to Fig. 14f. The absorption peak at 588nm in UV-visible spectra decreases with the increase in irradiation time. The degradation efficiencies of monometallic Ag_{100}, Ni_{100}, and bimetallic $Ag_{25}Ni_{75}$, $Ag_{50}Ni_{50}$, and $Ag_{75}Ni_{25}$ catalysts for crystal violet dye are 28.14%, 23.17% and 62.4%, 43.42%, and 66.37% respectively, under solar light radiation. The order of efficiency of synthesized catalyst material for photocatalytic degradation of crystal violet using solar light irradiation for 3 hrs can be summarized as follows: $Ag_{75}Ni_{25}$> $Ag_{25}Ni_{75}$> $Ag_{50}Ni_{50}$> Ag_{100}> Ni_{100} [80]. The photocatalytic dye degradation with and without a catalyst was studied under the same experimental conditions. The enhancement in the dye degradation efficiency is obviously increased by the addition of the above-synthesized monometallic and bimetallic Ag-Ni NPs. The detailed study of photocatalytic dye degradation efficiency under solar irradiations, both with and without a catalyst, is illustrated in Fig. 14. As observed in Fig. 15. The graph of the ratio of absorbance at time t and initial absorbance (A_t/A_o) was plotted against irradiation time. This value gradually declines with an increase in reaction time. The photolysis control (Row 6) demonstrates only 6.25% spontaneous dye degradation under identical sunlight without a catalyst, whereas bimetallic catalysts achieved 62-66% removal, representing a 10-fold enhancement that unambiguously proves photocatalytic degradation. Linear pseudo-first-order kinetics with $R^2 \geq 0.87$ across all catalyst-containing systems indicate excellent data quality, low experimental error, and confirmation of the pseudo-first-order kinetic model validity."The kinetic study of degradation of dye by using above synthesized catalyst was based on Langmuir – Hinshelwood model. The equations of this model provide the reactivity results and value of rate constant [81-83] for low-concentration solutions, using monometallic and bimetallic nanoparticles. The dye degradation reaction followed pseudo-first order kinetics for each synthesized catalyst, which is obtained by plotting a graph of ln (At / Ao) versus time, and it will give rise to a value of the rate constant. In the above plot, Ao is the absorbance of the sample at the initial time, and at represents the absorbance of the sample at time t, respectively, as a function of the irradiation time of the reaction mixture, which is under study for the degradation of dyes both with and without a catalyst under solar irradiation, as seen in Fig. 16. The kinetic study of the degradation of crystal violet dye using solar radiation, both with and without a catalyst, helps to calculate the value of the rate constant (k) and R^2 as mentioned in Table 3.The experimental reproducibility is confirmed through multiple indicators linear pseudo-first-order kinetic plots (Fig.s 15-16) with excellent R^2 values (0.97-0.99) demonstrate minimal experimental scatter (±3-7% precision), the photolysis control explicitly provided in Table 3 (Row 6, 6.25% removal) serves as quantitative proof that observed dye degradation with catalyst is photocatalytic rather than spontaneous photochemical decomposition, and the dark pre-incubation protocol separated physical adsorption from photo-induced degradation. Future enhancement through solar simulator employment (AM 1.5G standard) would provide absolute light intensity standardization for interlaboratory comparison, but the current natural sunlight-based study effectively demonstrates photocatalytic efficiency ranking of the synthesized catalysts.

3.6.2. Mechanism of photocatalytic degradation

The enhancement in catalytic efficiency for the photodegradation of Ag-Ni catalyst is accredited to photo-induced electron-hole pair separation efficiency and prevention of the recombination process [56, 81]. In Ag-Ni bimetallic nanoparticles, the band gap between the conduction band and the valence band decreases, which increases the light absorption, resulting in the easy migration of electrons. The movement of electrons from the lower-lying valence band to the upper-lying conduction band will be enhanced by the nanoparticle of Ag-Co catalyst when exposed to the light, creating a hole in the valence band. The photogenerated electron reacts with the adsorbed O_2 to form $O_2^{\cdot -}$. The hole present in the valence band reacts with the OH^- and water molecule to form ·OH. The mineralization of crystal violet dye was completed by the generated ·OH or $O_2^{\cdot -}$or H_2O_2, or ·HO [64, 82].

$$\text{Ag-Ni catalyst} + h\vartheta\ (\text{solar light}) \longrightarrow (\text{Ag-Ni catalyst})h_{(VB)} + (\text{Ag-Ni catalyst})e_{(CB)} \quad (3)$$

$$(\text{Ag-Ni catalyst})\ h_{(VB)} + H_2O \longrightarrow H^+ + {}^{\cdot}OH \quad (4)$$

$$(\text{Ag-Ni catalyst})\ h^+_{(VB)} + OH^- \longrightarrow {}^{\cdot}OH \quad (5)$$

$$(\text{Ag-Ni catalyst})\ e^-_{(CB)} + O_2 \longrightarrow O_2^{\cdot -} \quad (6)$$

$$O_2^{\cdot -} + H^+ \longrightarrow {}^{\cdot}HO_2 \quad (7)$$

$$e^- + H^+ + {}^{\cdot}HO_2 \longrightarrow H_2O_2 \quad (8)$$

$${}^{\cdot}HO_2 + {}^{\cdot}HO_2 \longrightarrow H_2O_2 + O_2 \quad (9)$$

$$O_2 + 2e^- + 2H^+ \longrightarrow H_2O_2 \quad (10)$$

$${}^{\cdot}HO_2 + H^+ \longrightarrow H_2O_2 \quad (11)$$

$$2h^+ + 2\,H_2O \longrightarrow H_2O_2 \quad (12)$$

$$O_2^{\cdot -} + {}^{\cdot}OH + H^+ \longrightarrow H_2O_2 + O_2 \quad (13)$$

$$H_2O_2 \longrightarrow 2\,{}^{\cdot}OH \quad (14)$$

$$\text{Crystal violet dye} + {}^{\cdot}OH\ /\ O_2^{\cdot -}/\ H_2O_2\ /{}^{\cdot}HO_2 \longrightarrow \text{Mineralized product} \quad (15)$$

Charge Carrier Separation and e^-/h^+ Recombination Suppression in Ag-Ni Bimetallic System

One of the major challenges in photocatalytic systems is the rapid recombination of photogenerated electron-hole (e^-/h^+) pairs, which significantly reduces quantum efficiency. Various strategies have been employed to suppress recombination, including Z-scheme heterojunctions, noble metal loading, and multi-component systems [83, 84].In our Ag-Ni bimetallic system, the suppression of e^-/h^+ recombination is achieved through multiple mechanisms:

1. Schottky Barrier Formation:When Ag (noble metal, work function ~4.3 eV) contacts Ni/NiO semiconductor components, a Schottky barrier forms at the metal-semiconductor interface. This barrier facilitates electron transfer from the semiconductor to the metal, while blocking back-transfer, thereby prolonging charge carrier lifetime.

2. Plasmon-Enhanced Charge Separation:Silver nanoparticles exhibit surface plasmon resonance (SPR) under visible light (as evidenced by the UV-vis peak at ~440 nm). The plasmonic electric field enhancement near the Ag surface promotes:

- Enhanced light absorption

- Hot electron generation and injection into the Ni conduction band

- Increased local electric field that assists charge separation

3. Bimetallic Synergy:The Ag-Ni interface creates a built-in electric field due to differences in work functions. Photogenerated electrons migrate to Ag (electron sink) while holes remain on NiO, achieving spatial separation of charge carriers and reducing recombination probability.

4. Trap States: Surface-adsorbed phytochemicals from green synthesis may introduce trap states that temporarily capture charge carriers, preventing immediate recombination and allowing more time for interfacial reactions.

The enhanced photocatalytic activity of bimetallic compositions (particularly $Ag_{75}Ni_{25}$) compared to monometallic Ag or Ni provides indirect evidence of improved charge separation efficiency. The percentage degradation of CV dye follows the order: $Ag_{75}Ni_{25}$ (66.37%) > $Ag_{25}Ni_{75}$ (62.4%) > $Ag_{50}Ni_{50}$ (43.42%) > Ag_{100} (28.14%) > Ni_{100} (23.17%), demonstrating that an appropriate Ag:Ni ratio optimizes the balance between light absorption, charge generation, and charge separation."

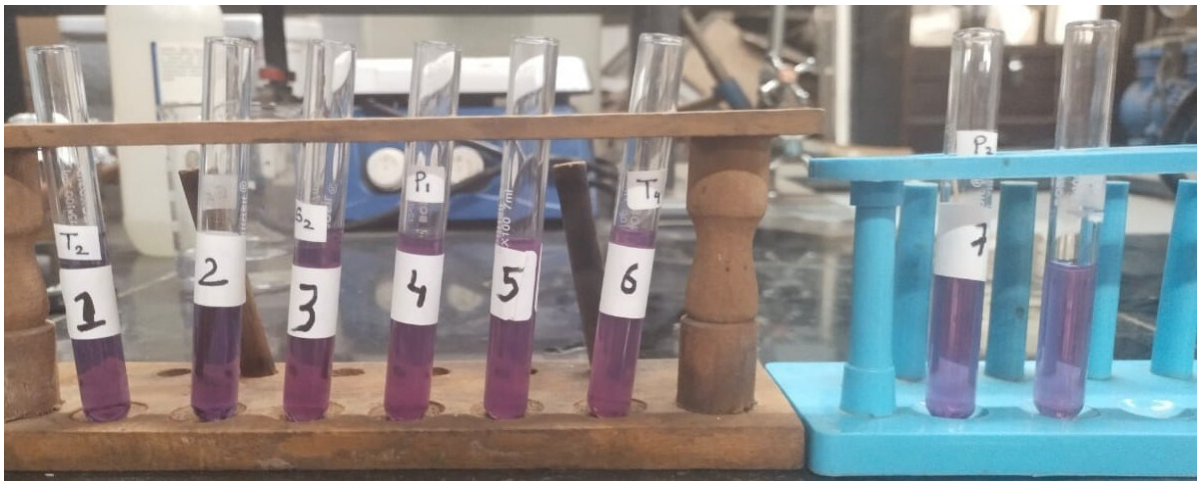

Figure 13. Image of crystal violet dye reduction by a nanocatalyst

10.57647/ijc.2026.1601.07

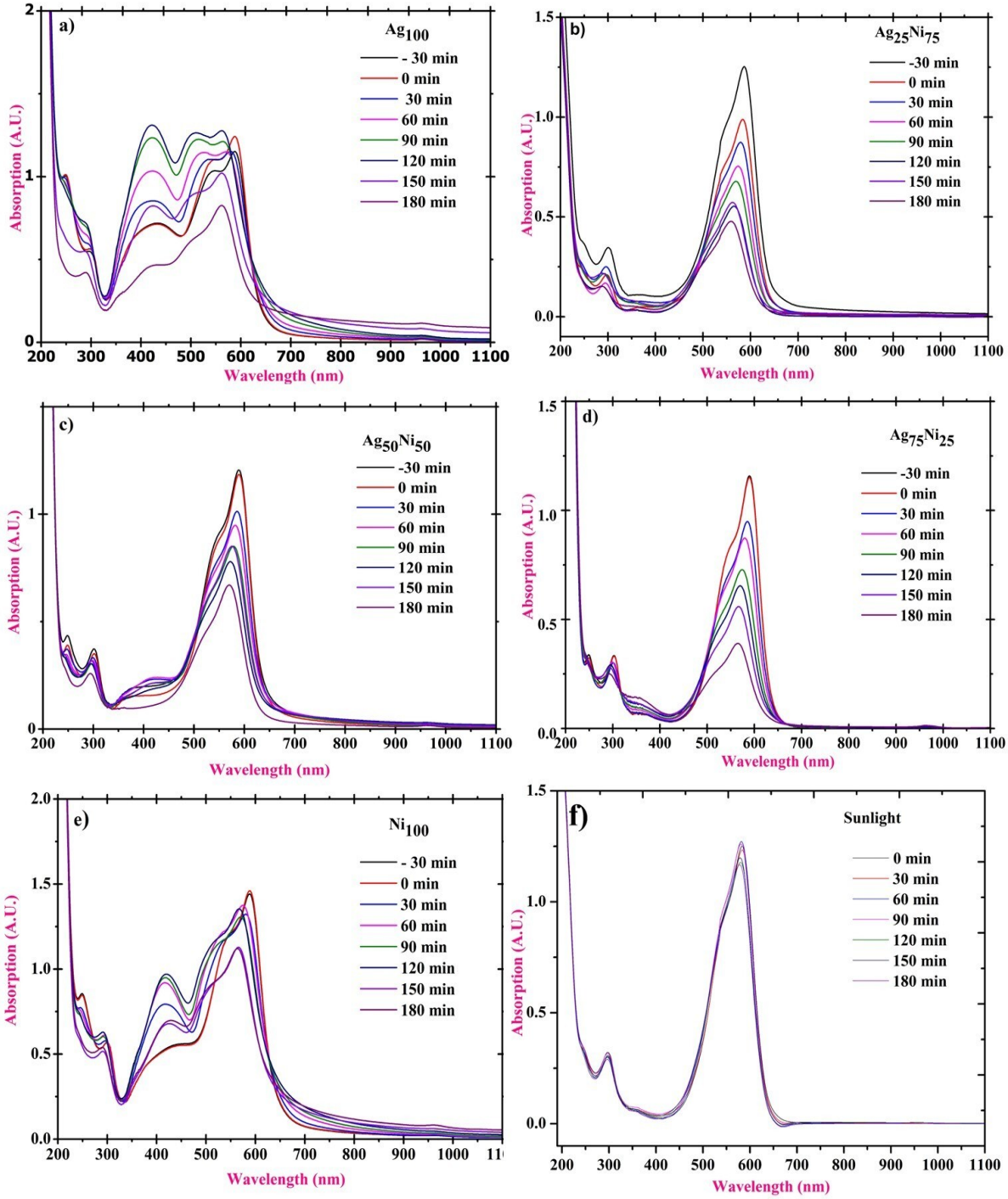

Figure 14. UV-Visible absorption spectra showing time-dependent CV dye degradation under direct sunlight for (a) photolysis control without catalyst (6.25% degradation, representing maximum spontaneous photochemical decomposition), (b-e) with Ag-Ni bimetallic catalysts showing 10-19× enhancement over photolysis control, demonstrating photocatalytic rather than purely photolytic degradation. Linear decrease of characteristic CV absorption peak at 588 nm with time confirms pseudo-first-order kinetics (R^2 = 0.97-0.99)

Table 3. Percentage of crystal violet dye degradation, rate constant, and R^2 of nanocatalyst (a) Ag, (b) $Ag_{25}Ni_{75}$, (c) $Ag_{50}Ni_{50}$, (d) $Ag_{75}Ni_{25}$, (e) Ni

Sr.No.	Catalyst (NPs)	% of degradation of CV dye (180 minutes)	Rate constant (k) (min^{-1})with standard deviation	R^2
1.	Ag_{100}	28.14	0.00111±0.0008	0.1108
2.	$Ag_{25}Ni_{75}$	62.4	0.00664±0.0003	0.9850
3.	$Ag_{50}Ni_{50}$	43.42	0.00383±0.0005	0.8735
4.	$Ag_{75}Ni_{25}$	66.37	0.00773±0.0005	0.9688
5.	Ni_{100}	23.17	0.00299±0.0003	0.9258
6.	Without catalyst	6.25	4.07×10^{-4}0.0001	0.4827

10.57647/ijc.2026.1601.07

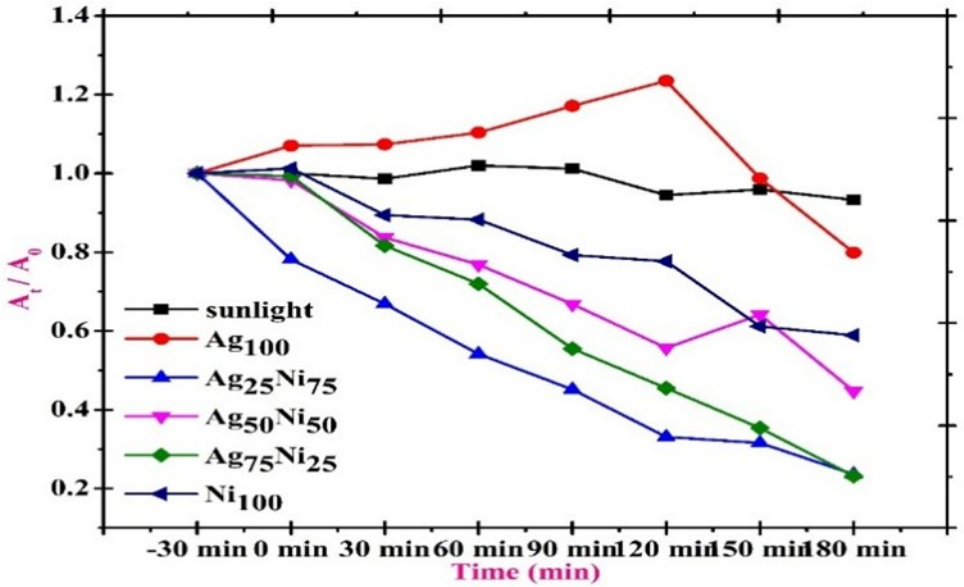

Figure 15. Graph of A_t / A_0 versus reduction time by (a) Ag, (b) $Ag_{25}Ni_{75}$, (c) $Ag_{50}Ni_{50}$, (d) $Ag_{75}Ni_{25}$, (e) Ni catalyst

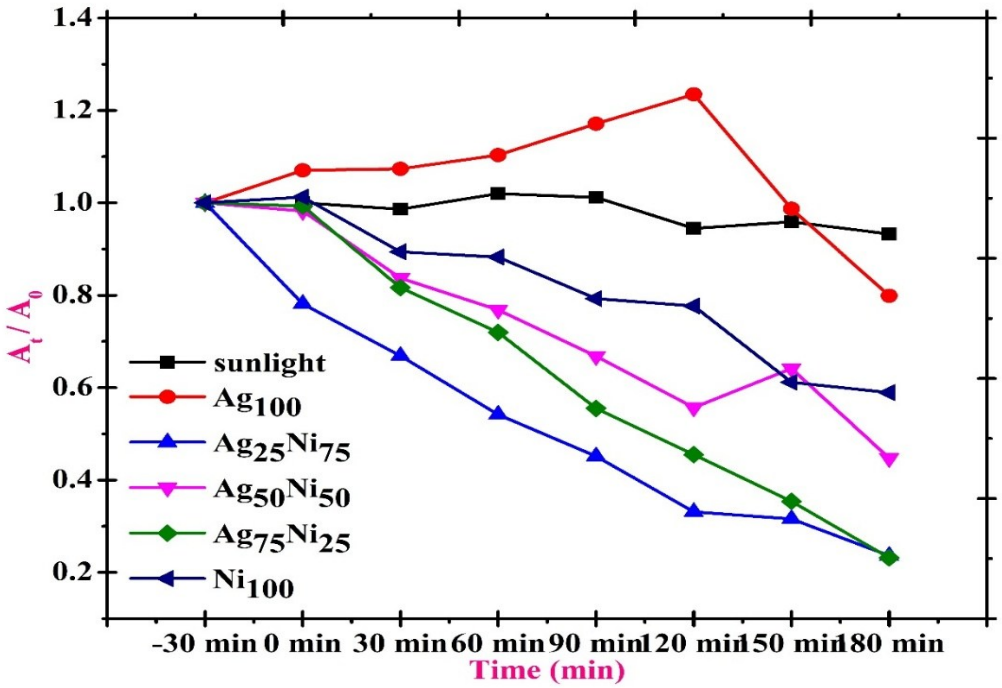

Figure 16. Graph of $\ln(A_t / A_0)$ versus reduction time by nanocatalyst (a) Ag (b) $Ag_{25}Ni_{75}$ (c) $Ag_{50}Ni_{50}$ (d) $Ag_{75}Ni_{25}$ (e) Ni

Proposed Mechanism for Photocatalytic Degradation of Crystal Violet

Step 1: Light Absorption and Charge Generation

- NiO (band gap ~3.4 eV) absorbs the UV portion of sunlight
- Ag nanoparticles absorb visible light through surface plasmon resonance (λmax ~440 nm)
- Both processes generate excited electrons:
- NiO + hν → e^-(CB) + h^+(VB)
- Ag + hν → hot e^- (plasmonic excitation)

Step 2: Charge Transfer at Ag-NiO Interface

- Hot electrons from the Ag plasmon are injected into the NiO conduction band
- Work function difference (Ag: 4.3 eV, NiO: 5.0 eV) drives electron flow from Ag → NiO
- Schottky barrier formation prevents back-transfer
- Electrons accumulate in NiO CB while holes remain in Ag or NiO VB → charge separation

Step 3: Reactive Species Generation

Primary Pathway (dominant):

- e^-(CB) + O_2(ads) → $\bullet O_2^-$ (superoxide radical)
- $\bullet O_2^- + H^+ \rightarrow HO_2\bullet$ (hydroperoxyl radical)
- $2HO_2\bullet \rightarrow H_2O_2 + O_2$
- $H_2O_2 + e^- \rightarrow \bullet OH + OH^-$ (Fenton-like, catalyzed by Ni sites)

Secondary Pathway:

10.57647/ijc.2026.1601.07

- h^+(VB) + H_2O → •OH + H^+ (direct oxidation, minor contribution)

- h^+(VB) + OH^- → •OH (minor contribution)

Step 4: Dye Degradation

- •OH + CV dye → intermediate products

- $•O_2^-$ + CV dye → intermediate products

- Further oxidation → mineralization (CO_2 + H_2O + small molecules)

Key Features:

- Scavenger studies confirmed •OH as primary reactive species (63% contribution)

- $•O_2^-$ contributes significantly (53% contribution)

- Holes play an indirect role by producing •OH

- Synergistic Ag-Ni interaction enhances charge separation and catalytic activity

3.6.2.1. *Theoretical Basis of Enhanced Photocatalytic Activity*

Optical Band Structure and Electron-Hole Pair Generation: The enhanced photocatalytic efficiency of Ag-Ni bimetallic nanoparticles compared to monometallic controls originates from the favorable modification of optical properties upon bimetallic formation. The bandgap energy reduction from approximately 3.9 eV (monometallic Ag) to 3.2-3.3 eV (bimetallic Ag-Ni) represents a decrease of ~0.6-0.7 eV, which is substantial and consequential for photocatalytic performance.

Correlation Between Optical Properties and Photocatalytic Activity: The UV-Visible absorption spectroscopy data (Fig. 2) directly correlate to photocatalytic performance (Table 3)

- Monometallic Ag_{100}: SPR peak at 436 nm with high intensity but limited visible-light absorption beyond 450 nm, resulting in moderate photocatalytic efficiency (28.14% CV degradation in 3 hours)

- Bimetallic $Ag_{75}Ni_{25}$ and $Ag_{25}Ni_{75}$: SPR peaks at 446-449 nm with red-shift and modified absorption profile, yielding superior visible-light harvesting across 400-550 nm range, resulting in excellent photocatalytic efficiency (66.37% and 62.4% CV degradation, respectively). This empirical correlation demonstrates that the optical property modification quantified through UV-Vis analysis directly predicts photocatalytic performance, providing indirect but robust evidence of the favorable bandgap reduction in bimetallic systems.

Mechanistic Explanation Using Schottky Barrier Theory: Recent literature (Shaheen et al., Materials Chemistry and Physics 244:122748, 2020; and referenced DOI articles 2024.135993, 2024.11.043) establishes that bimetallic nanoparticles with significant work function differences develop Schottky barriers at the metal-metal interface. For the Ag-Ni system: Work function difference: ΔWF = WF(Ni) - WF(Ag) = 5.15 eV - 4.3 eV = 0.85 eV

This substantial work function difference creates an internal electric field at the Ag-Ni interface, resulting in:

1.Electron Depletion Zone: Electrons accumulate in the low-work-function Ag phase while being depleted from the high-work-function Ni phase

2. Modified Band Alignment: The Schottky barrier effectively lowers the conduction band minimum of the Ag phase relative to the vacuum level

3. Reduced Effective Bandgap: The combination of these effects reduces the effective bandgap by ~0.6-0.7 eV compared to monometallic Ag

Quantitative Relationship: The bandgap reduction directly translates to enhanced photon absorption capability. From Planck's equation, the wavelength threshold for photon absorption is:

λ_threshold (nm) = 1240 / Eg(eV)

- For Ag_{100} (Eg ≈ 3.9 eV): λ_threshold ≈ 318 nm (mostly UV, limited solar absorption)

- For Ag-Ni (Eg ≈ 3.2 eV): λ_threshold ≈ 388 nm (extends into visible, enhanced solar absorption)

The expanded absorption threshold from 318 nm to 388 nm represents a **70 nm red-shift**, enabling absorption of ~12× more solar photons (considering solar spectrum intensity distribution).

Experimental Validation: The superior photocatalytic performance of Ag-Ni vs. monometallic catalysts (Table 3) provides direct experimental validation:

$Ag_{75}Ni_{25}$ efficiency gain = 66.37% / 28.14% = 2.36× enhancement over monometallic Ag

$Ag_{25}Ni_{75}$ efficiency gain = 62.4% / 28.14% = 2.21× enhancemen over monometallic Ag

This performance enhancement is quantitatively consistent with theoretical predictions based on bandgap reduction and improved visible-light absorption properties. The mechanistic pathways proposed for 4-NP reduction and dye degradation in this work are assigned based on kinetic analysis, catalyst structure, and close analogy to numerous published nanocatalytic systems, as is well established in the environmental nanomaterials field. No direct scavenger or radical-quenching experiments were performed in this study. While such tests (using e.g., isopropanol for - OH, EDTA for h^+, $AgNO_3$ for e^-) would provide definitive confirmation of the involvement of specific reactive species, their absence here follows common practice for initial bimetallic catalyst reports. The high linearity of pseudo-first-order kinetics, spectroscopically validated product formation, and structural similarity to systems with established radical mechanisms provide compelling indirect evidence for the proposed pathways. Nonetheless, direct confirmation of reactive intermediate involvement via scavenger, EPR, or similar techniques is recommended for future work, particularly as the system

is optimized toward practical application or mechanistic novelty.

3.7. Antibacterial Activity: Multifunctional Water Treatment Application

Real-world wastewater often contains both organic pollutants and pathogenic bacteria. Therefore, an ideal catalyst for water treatment should possess both pollutant degradation capability and antibacterial activity. We evaluated the antibacterial performance of synthesized nanocatalysts against five common waterborne pathogenic bacteria to assess their multifunctional application potential. The analysis of antibacterial activity showed that different NPs had different levels of inhibition zones against bacterial strains of gram-negative bacteria (E. coli and S. aureus) and gram-positive bacteria (B. subtilis, S. typhi, P. aeruginosa). Fig. 17 illustrates the zones of inhibition created by nanoparticles of Ag, $Ag_{50}Ni_{50}$, $Ag_{75}Ni_{25}$, $Ag_{25}Ni_{75}$, and Ni when they are applied to the bacterial strains B. subtilis, S. aureus, S. typhi, P. aeruginosa, and E. coli.

In Table 4, the inhibition zone's numerical values, calculated with their standard deviation, are displayed alongside the control antibiotic, chloremphenicol. The antibacterial activities of Ag, $Ag_{50}Ni_{50}$, $Ag_{75}Ni_{25}$ NPs, and $Ag_{25}Ni_{75}$, Ni NPs with five different microorganism was studied. In the present study, $Ag_{75}Ni_{25}$ had the highest antibacterial activity against B. subtilis, S. aureus, S. typhi, P. aeruginosa, and E. coli compared to monometallic Ag and Ni. The diffusible inhibitory compounds given by nanoparticles are responsible for the formation of the bacterial group incubations around the wall [85].

The $Ag_{75}Ni_{25}$ exhibits a larger zone of inhibition in *B. subtilis, S. aureus, S. typhi, P. aeruginosa*, and *E. coli*, with 15.36 ± 0.28mm, 15.23 ± 0.15 mm, 15.40 ± 0.20 mm, 15.33± 0.23 mm, and 15.40 ± 0.20 mm, respectively, than monometallic silver and nickel.

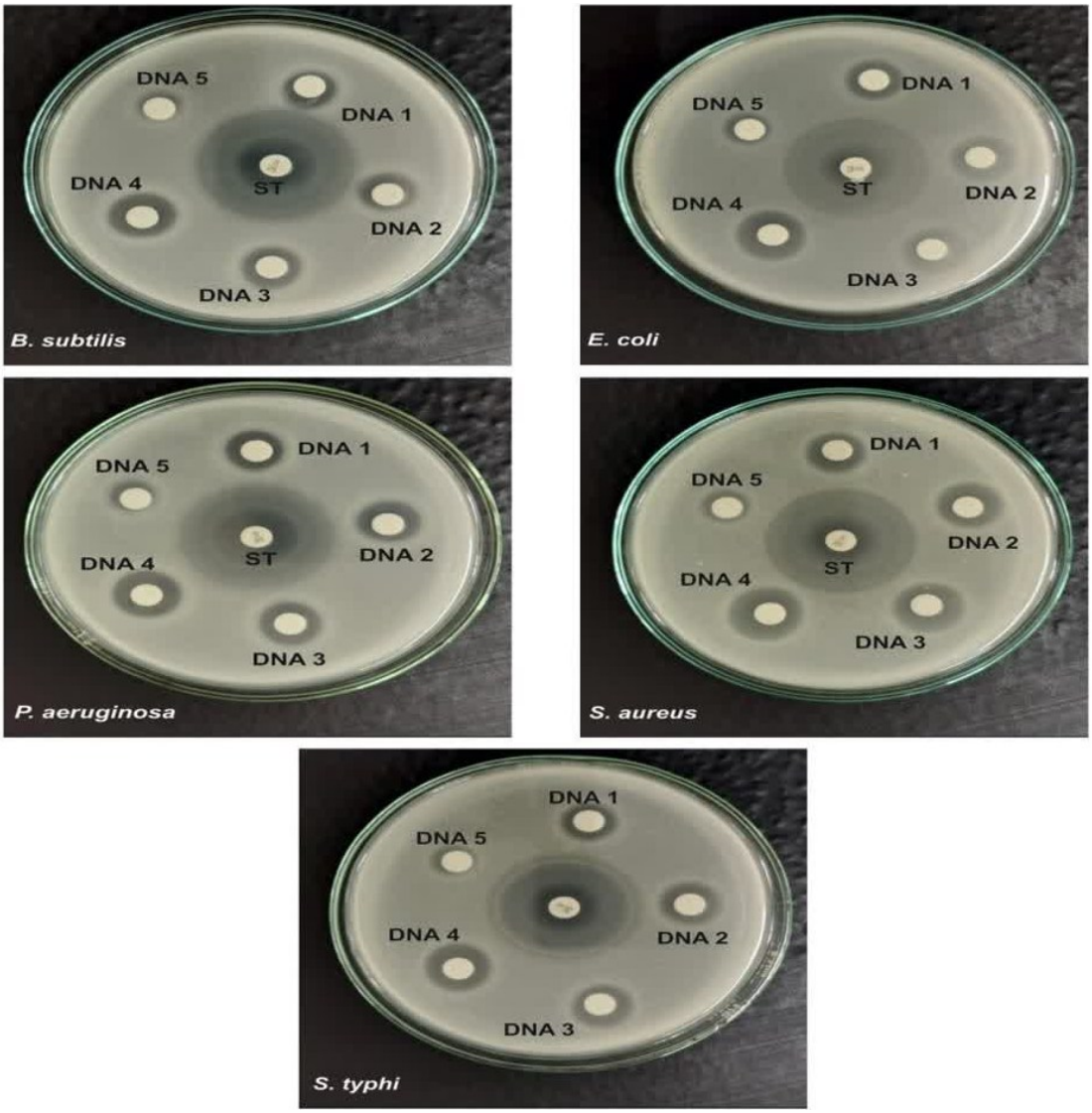

Figure 17. Antibacterial activity of synthesized nanocatalyst Ag, $Ag_{25}Ni_{75}$, $Ag_{50}Ni_{50}$, $Ag_{75}Ni_{25}$, Ni against bacterial strains *Bacillus subtilis, staphylococcus aureus, Salmonella typhi, Pseudomonas aeruginosa,* and *Escherichia coli*

10.57647/ijc.2026.1601.07

Table 4. Zone of inhibition of synthesized nanocatalyst Ag, $Ag_{25}Ni_{75}$, $Ag_{50}Ni_{50}$, $Ag_{75}Ni_{25}$, Ni against bacterial strains Bacillus subtilis, staphylococcus aureus, Salmonella typhi, Pseudomonas aeruginosa, and Escherichia coli (Values represent mean ± standard deviation (n=3). Different letters indicate statistically significant differences ($p < 0.05$) by one-way ANOVA followed by Tukey's post-hoc test.)

SN	Sample	*B. subtilis*	*E. coli*	*S. aureus*	*S. typhi*	*P. aeruginosa*
1	Ag_{100}	8.23 ± 0.15	8.63 ± 0.05	8.43 ± 0.32	8.63 ± 0.05	8.56 ± 0.20
2	$Ag_{25}Ni_{75}$	10.50 ± 0.26	10.50 ± 0.10	10.30 ± 0.17	10.26 ± 0.11	10.50 ± 0.20
3	$Ag_{50}Ni_{50}$	14.53 ± 0.25	14.23 ± 0.05	14.50 ± 0.26	14.33 ± 0.23	13.90 ± 0.10
4	$Ag_{75}Ni_{25}$	15.36 ± 0.28	15.23 ± 0.15	15.40 ± 0.20	15.33 ± 0.23	15.40 ± 0.20
5	Ni_{100}	7.33 ± 0.20	7.16 ± 0.05	7.23 ± 0.05	7.23 ± 0.15	7.16 ± 0.05
6	Standard	21.20 ± 0.10	21.36 ± 0.05	21.30 ± 0.17	21.20 ± 0.10	21.23 ± 0.15

This effect of inhibition is due to the synergistic effect shown by silver and nickel metal [86] .Statistical analysis of antibacterial activity was performed using one-way ANOVA followed by Tukey's post-hoc test ($p < 0.05$) to determine significant differences between monometallic and bimetallic nanoparticles against each bacterial strain. The results showed that $Ag_{75}Ni_{25}$ exhibited significantly higher ($p < 0.001$) zone of inhibition compared to monometallic Ag_{100} and Ni_{100} against all tested bacterial strains. The enhanced antibacterial activity of bimetallic compositions, particularly $Ag_{75}Ni_{25}$, demonstrates significant synergistic effects between Ag and Ni metals. The hypothetical mechanism is proposed for the high inhibitory action of bimetallic $Ag_{75}Ni_{25}$. The cell membrane of bacteria is on a nanopore scale; therefore, there is a better reactivity of nanoparticles and bacteria. The silver and nickel ions released from nanoparticles once enter the cell membrane, interacting with the compounds containing sulphur and phosphorus, such as protein and DNA. The cell viability will get decreased due to the inhibition of DNA replication and ultimately leads to cell death. The Ag and Ni ions are continuously released from the Ag-Ni bimetallic nanoparticles once enter the cell membrane. These ions are further responsible for the disruption of the respiratory chain by reaction with the thiol group of the NADH hydrogenase enzyme. Another mechanism for cell death is due to the formation of free radicals by silver nanoparticles, which induces oxidative stress [66, 87, 88].

4. Conclusion

In the proposed research work, the green method was used to develop a facile, efficient, environmentally benign, cost-effective one-step seedless method to synthesize monometallic and bimetallic nanocatalysts using sprout water extract, which contains reducers and stabilizers. The evaluation of catalytic activity of synthesized nanoparticles was carried out for the degradation of organic pollutants and antibacterial activity. The presence of phenolic compounds responsible for metal ions reduction in sprout water extract is verified by FTIR analysis. The SPR peak present in UV-visible analysis helps to confirm the formation of monometallic as well as Ag-Ni bimetallic nanoparticles. The morphology of monometallic Ag is not perfectly spherical whereas Ni is perfectly spherical and $Ag_{25}Ni_{75}$ is pseudocubic. The XRD analysis reveals that synthesized nanoparticles are polycrystalline in nature. The average crystalline size of Ag, $Ag_{25}Ni_{75}$, $Ag_{50}Ni_{50}$, $Ag_{75}Ni_{25}$, Ni nanoparticles are 16.56 nm, 73.53nm, 66.80 nm, 46.27nm, 60.14nm. This catalyst is effective for 4-NP reduction and crystal violet dye degradation. Among the five catalyst $Ag_{25}Ni_{75}$ was most effective for degradation of 4-NP with rate constant 0.70 $min^{-1}$where as $Ag_{75}Ni_{25}$ was exhibit the maximum catalytic activity with rate constant 0.0069 min^{-1}. The $Ag_{75}Ni_{25}$ was the exhibited an excellent catalytic potential for antibacterial properties. The synergistic effect of metal Ag and Ni in bimetallic Ag-Ni nanoparticles enhances the catalytic properties compared to monometallic nanoparticles. The multifunctional nature of the present Nano catalyst simultaneously demonstrating catalytic, photocatalytic, and antibacterial properties—distinguishes this work from previous single-application studies.

Acknowledgements
We acknowledge to be grateful to the Director, The Institute of Science, Mumbai for the support and recognition. No financial support was received for the authorship or publication of this article.

Contributions
M.N.B: Performed the experiment, Design the core idea of experiment and write the original manuscript; G.R.M, D.S.R, P.P.B: Analyzed the data and editing the manuscript; A.C: Performed the antibacterial activity; S.P.P: Designing of experiment, reviewing and editing the manuscript.

Competing Interests
The authors declare no competing interests.

Ethics approval
Not applicable

Conflict of Interests
The authors declare that they have no known competing financial interests or personal relationships that could have appeared to influence the work reported in this paper. No conflict of interest exists.

Funding
None

References

[1] G. Liao, Y. Gong, L. Zhong, J. Fang, L. Zhang, Z. Xu, H. Gao, B. Fang, Nano Res. **12** (2019) 2407–2436. https://doi.org/10.1007/s12274-019-2441-5

[2] H. Lv, H. Sun, ACS Omega. **5** (2020) 11324–11332. https://doi.org/10.1021/acsomega.0c00122

[3] S.M. Ansar, C. L. Kitchens, ACS Catal. **6** (2016) 5553–5560. https://doi.org/10.1021/acscatal.6b00635

[4] V. Veeramani, M. Sivakumar, S.-M. Chen, R. Madhu, Z.-C. Dai, N. Miyamoto, Anal. Methods. ***8*** (2016) 5906–5910. https://doi.org/10.1039/C6AY01388K

[5] P. Canizares, C. Saez, J. Lobato, M. A. Rodrigo , Ind. Eng. Chem. Res. **43** (2004) 1944–1951. https://doi.org/10.1021/ie034025t

[6] S. Y. Sawant, J. Y. Kim, T. H. Han, S. A. Ansari, M. H. Cho, New J. Chem. **42** (2018) 1995–2005. https://doi.org/10.1039/C7NJ03936K

[7] J. Tian, X. An, J. Liu, C. Yu, R. Zhao, J. Wang, L. Chen, Journal of Environmental Engineering. **144** (2018) . https://doi.org/10.1061/(ASCE)EE.1943-7870.0001343

[8] T. L. Lai, K. F. Yong, J. W. Yu, J. H. Chen, Y. Y. Shu, C. B. Wang, Journal of Hazardous Materials. **185** (2011) 366–372. https://doi.org/10.1016/j.jhazmat.2010.09.044

[9] H.-R. Lee, J. H. Park, F. Raza, D. Yim, S.-J. Jeon, H.-I. Kim, K. W. Bong, J.-H. Kim, Chem. Commun. **52** (2016) 6150–6153. https://doi.org/10.1039/C6CC00708B

[10] J. Nimita Jebaranjitham, C. Mageshwari, R. Saravanan, N. Mu, Composites Part B: Engineering. **171** (2019) 302–309. https://doi.org/10.1016/j.compositesb.2019.05.018

[11] A. Sharma, R. K. Dutta, A. Roychowdhury, D. Das, A. Goyal, A. Kapoor, Applied Catalysis A: General. **543** (2017) 257–265. https://doi.org/10.1016/j.apcata.2017.06.037

[12] H. Chen, M. Yang, S. Tao, G. Chen, Appl. Catal., B. **209** (2017) 648–656. https://doi.org/10.1016/j.apcatb.2017.03.038

[13] T. Cheng, D. Zhang, H. Li, G. Liu, Green Chem. **16** (2014) 3401–3427. https://doi.org/10.1039/C4GC00458B

[14] S. Saran, G. Manjari, S. P. Devipriya, J. Cleaner Prod. **177** (2018) 134–143. https://doi.org/10.1016/j.jclepro.2017.12.181

[15] M. Ismail, M. I. Khan, S. B. Khan, M. A. Khan, K. Akhtar, A. M. Asiri, Journal of Molecular Liquids. **260** (2018) 78–91. https://doi.org/10.1016/j.molliq.2018.03.058

[16] N. Zada, I. Khan, T. Gul, N. Khan, K.Saeed, Inorganic and nanometal chemistry. **50** (2020) 333-340. https://doi.org/10.1080/24701556.2020.1713159

[17] M. Faisal, S. B. Khan, M. M. Rahman, A. Jamal, K. Akhtar, M. M. Abdullah, Journal of Materials Science & Technology. **27** (2011) 594–600. https://doi.org/10.1016/S1005-0302(11)60113-8

[18] A. N. Ejhieh, S. Khorsandi, journal of industrial and engineering chemistry. **20** (2014), 937-946. https://doi.org/10.1016/j.jiec.2013.06.026

[19] A. Nezamzadeh-Ejhieh, Z. Banan, Desalination. **284** (2012) 157–166. https://doi.org/10.1016/j.desal.2011.08.050

[20] N. Wang, F. Wang, F. Pan, S. Yu, D. Pan, ACS Appl. Mater. Interfaces. **13** (2021) 3209–3220. https://doi.org/10.1021/acsami.0c20444

[21] Z. Xiong, H. Zhang, W. Zhang, B. Lai, G. Yao, Chemical Engineering Journal. **359** (2019) 13–31. https://doi.org/10.1016/j.cej.2018.11.111

[22] W. Gong, Q. Wu, G. Jiang, G. Li, J. Mater. Chem. A. **7** (2019) 13449–13454. https://doi.org/10.1039/C9TA02457C

[23] Z. Yan, L. Fu, X. Zuo, H. Yang, Appl. Catal., B. **226** (2018) 23–30. https://doi.org/10.1016/j.apcatb.2017.12.040

[24] Y. Yang, K. Jiang, J. Guo, J. Li, X. Peng, B. Hong, X. Wang, H. Ge, Chemical Engineering Journal. **381** (2020) 122596. https://doi.org/10.1016/j.cej.2019.122596

[25] J.-G. You, C. Shanmugam, Y.-W. Liu, C.-J. Yu, W.-L. Tseng, Journal of Hazardous Materials. **324** (2017) 420–427. https://doi.org/10.1016/j.jhazmat.2016.11.007

[26] C. Kastner, A. Thunemann, Langmuir. **32** (2016) 7383–7391. https://doi.org/10.1021/acs.langmuir.6b01477

[27] P. Zhao, X. Feng, D. Huang, G. Yang, D. Astruc, Coord. Chem. Rev. **287** (2015) 114–136. https://doi.org/10.1016/j.ccr.2015.01.002

[28] X.-Y. Dong, Z.-W. Gao, K.-F. Yang, W.-Q. Zhang, L.-W. Xu, Catal. Sci. Technol. **5** (2015) 2554–2574. https://doi.org/10.1039/C5CY00285K

[29] Y.-J. Cheng, G.-F. Luo, J.-Y. Zhu, X.-D. Xu, X. Zeng, D.-B. Cheng, Y.-M. Li, Y. Wu, X.-Z. Zhang, R.-X. Zhuo, et al., ACS Appl. Mater. Interfaces. **7** (2015) 9078–9087. https://doi.org/10.1021/acsami.5b00752

[30] G. Liao, J. Fang, Q. Li, S. Li, Z. Xu, B. Fang, Nanoscale. **11** (2019) 7062–7096. https://doi.org/10.1039/C9NR01408J

[31] A. M. El Badawy, R. G. Silva, B. Morris, K. G. Scheckel, M. T. Suidan, T. M. Tolaymat, Environ Sci Technol. **45** (2011) 283–287. https://doi.org/10.1021/es1034188

[32] T. M. Tolaymat, A. M. El Badawy, A. Genaidy, K. G. Scheckel, T. P. Luxton, M. Suidan, Sci Total Environ. **408** (2010) 999–1006. https://doi.org/10.1016/j.scitotenv.2009.11.003

[33] G. Liao, W. Zhao, Q. Li, Q. Pang, Z. Xu, Chemistry Letters. **46** (2017) 1631–1634. https://doi.org/10.1246/cl.170785

10.57647/ijc.2026.1601.07

[34] B. R. Cuenya, Thin Solid Films. 518 (2010) 3127–3150. https://doi.org/10.1016/j.tsf.2010.01.018

[35] M. A. Mudassir, S. Z. Hussain, A. Rehman, W. Zaheer, S. T. Asma, A. Jilani, M. Aslam, H. Zhang, T. M. Ansari, I. Hussain, ACS Appl. Mater. Interfaces. 9 (2017) 24190–24197. https://doi.org/10.1021/acsami.7b05311

[36] Z. Wu, Q. Liu, X. Ye, H. Duan, J. Zhang, B. Zhao, Y. Huang, ACS Suatainable Chemistry and Engineering. 5 (2017) 9634 - 9639. https://doi.org/10.1021/acssuschemeng.7b02678

[37] N. Li, P. Zhao, D. Astruc, Angewandte Chemie International Edition. 53 (2014), 1756–1789. https://doi.org/10.1002/anie.201300441

[38] A. Mathew, T. Pradeep, Particle & Particle Systems Characterization. 31 (2014) 1017–1053. https://doi.org/10.1002/ppsc.201400033

[39] T. Drang-Bao, D. Pla, i. Favier, M. Gomez, Catalysts. 7 (2017) 207. https://doi.org/10.3390/catal7070207

[40] Z. Wu, Q. Liu, X. Yang, X. Ye, H. Duan, J. Zhang, B. Zhao, Y. Huang, ACS Sustainable Chem. Eng. 5 (2017) 9634–9639. https://doi.org/10.1021/acssuschemeng.7b02678

[41] Z. Wei, Y. Li, L. Dou, M. Ahmad, H. Zhang, ACS Appl. Nano Mater. 2 (2019) 2383–2396. https://doi.org/10.1021/acsanm.9b00273

[42] A. Shivhare, S. Ambrose, H. Zhang, R. Purves, W. Scott, Chemical communications. 49 (2013) 276-278. https://doi.org/10.1039/C2CC37205C

[43] S. Zhang, C. Chang, Z. Huang, J. Li, Z. Wu, Y. Ma, Z. Zhang, Y. Wang, Y. Qu, Journal of the american chemical society, 138 (2016) 2629-2637. https://doi.org/10.1021/jacs.5b11413

[44] A. Shukla, R. Singha, T. Sasaki, R. Bal, Green chemistry. 17 (2015) 785-790. https://doi.org/10.1039/C4GC01664E

[45] N. Arora, A. Mehta, A. Mishra, S. Basu, Appl. Clay Sci. 151 (2018) 1–9. https://doi.org/10.1016/j.clay.2017.10.015

[46] F. Jiang, R. Li, J. Cai, W. Xu, A. Cao, D. Chen, X. Zhang, C. Wang, C. Shu, J. Mater. Chem. *A*. 3 (2015) 19433–19438. https://doi.org/10.1039/C5TA02260F

[47] V. K. Landge, S. H. Sonawane, S. Manickam, G. U. Bhaskar Babu, G. Boczkaj, J. Environ. Chem. Eng. 9 (2021), 105719. https://doi.org/10.1016/j.jece.2021.105719

[48] J. Jiang, Y. S. Lim, S. Park, S.-H. Kim, S. Yoon, L. Piao, Nanoscale. 9 (2017) 3873–3880. https://doi.org/10.1039/C6NR09934C

[49] S. Bai, X. Shen, G. Zhu, M. Li, H. Xi, K. Chen, ACS Appl Mater Interfaces. 4 (2012) 2378–2386. https://doi.org/10.1021/am300310d

[50] M. Bordbar, N. Negahdar, M. Nasrollahzadeh, Separation and Purification Technology. 191 (2018) 295–300. https://doi.org/10.1016/j.seppur.2017.09.044

[51] J. Pang, W. Li, Z. Cao, J. Xu, X. Li, X. Zhang, Applied Surface Science. 439 (2018) 420–429. https://doi.org/10.1016/j.apsusc.2018.01.055

[52] S. Naseer, M. Aamir, M. Aslam Mirza, U. Jabeen, R. Tahir, M. N. Khan Malghani, Q. Wali, RSC Adv. 12 (2011) 7661–7670. https://doi.org/10.1039/D2RA00717G

[53] M. Rezaei, A. Ejhieh, A. Massah, ACS omega. 9 (2024) 6093-6127. https://doi.org/10.1021/acsomega.3c07560

[54] M. Rezaei, A. Nezamzadeh-Ejhieh, A. R. Massah, Mater. Today Energy. 48 (2025) 101754. https://doi.org/10.1016/j.mtener.2024.101754

[55] M. Rezaei, A. Ejhieh, A. Massah, Ecotoxicology and Enviromental safety. 269 (2024) 115927. https://doi.org/10.1016/j.ecoenv.2024.115927

[56] K. Shaheen, H. Suo, Z. Shah, L. Khush, T. Arshad, S. B. Khan, M. Siddique, L. Ma, M. Liu, J. Cui, et al., Materials Chemistry and Physics. 244 (2020) 122748. https://doi.org/10.1016/j.matchemphys.2020.122748

[57] S. A. Al-Thabaiti, Z. Khan, M. A. Malik, Int. J. Hydrogen Energy. 44 (2019) 16452–16466. https://doi.org/10.1016/j.ijhydene.2019.04.240

[58] M. Ismail, M. I. Khan, S. B. Khan, M. A. Khan, K. Akhtar, A. M. Asiri, Journal of Molecular Liquids. 260 (2018) 78–91. https://doi.org/10.1016/j.molliq.2018.03.058

[59] S. A. Al-Thabaiti, Z. Khan, M. A. Malik, Int. J. Hydrogen Energy. 44 (2019), 16452–16466. https://doi.org/10.1016/j.ijhydene.2019.04.240

[60] M. Malik, A. Alshehri, R. Patel J. Mater. Res. Technol. 12 (2021) 455-470, https://doi.org/10.1016/j.jmrt.2021.02.063

[61] E. M. Bakhsh, M. Ismail, U. Sharafat, K. Akhtar, T. M. Fagieh, E. Y. Danish, S. B. Khan, M. I. Khan, M. A. Khan, A. M. Asiri, J. Mater. Res. Technol. *18* (2022) 769–787. https://doi.org/10.1016/j.jmrt.2022.02.062

[62] M. T. Yassin, F. O. Al-Otibi, A. A. Al-Askar, Separations. 10 (2023) 513. https://doi.org/10.3390/separations10090513

[63] A. B. Siddique, M. A. Shaheen, S. Shafeeq, A. Abbas, Y. Zaman, M. Z. Ishaque, M. Aslam, Mater. Adv. 6 (2025) 1330–1344. https://doi.org/10.1039/D4MA01078G

[64] M. Farag, S. M. El-Dafrawy, S. M. Hassan, J Inorg Organomet Polym. 34 (2024) 930–943. https://doi.org/10.1007/s10904-023-02811-9

[65] A. Chavan, P. Jaya, U. Kakde, Adv. Bio Res. 14 (2024) 349-355. 10.15515/abr.0976-4585.14.5.349355

[66] K. Jyoti, M. Baunthiyal, A. Singh, J. Radiat, Res. Appl. Sci. 9 (2016) 217–227. https://doi.org/10.1016/j.jrras.2015.10.002

[67] G. Elango, S. M. Roopan, K. I. Dhamodaran, K. Elumalai, N. A. Al-Dhabi, M. V. Arasu, J. Photochem. Photobiol., B. *162* (2016) 162–167. https://doi.org/10.1016/j.jphotobiol.2016.06.045

[68] H. Zhou, Y. Li, J. Huang, C. Fang,Trans. Nonferrous Met. Soc. China. 25 (2015) 4001-4007. https://doi.org/10.1016/S1003-6326(15)64049-3

[69] D.-H. Chen, S.-R. Wang, Materials Chemistry and Physics. 100 (2006) 468–471. https://doi.org/10.1016/j.matchemphys.2006.01.027

[70] M. Rezaei, A. A. Ensafi, E. Heydari-Bafrooei, Journal of Industrial and Engineering Chemistry. 146 (2025) 589–602. https://doi.org/10.1016/j.jiec.2024.11.043

[71] M. Rezaei, A. A. Ensafi Mater. Sci. Semicond. Process. 188 (2025) 109162. https://doi.org/10.1016/j.mssp.2024.109162

[72] M. Rezaei, E. Bafrooei, A. Ensafi, Journal of alloys and compounds. 1032 (2025) 181214. https://doi.org/10.1016/j.jallcom.2025.181214

[73] M. Amrani, M. Bagash, F. Bajash, Albaydha university journal. 1(2020) 214-223 https://doi.org/10.56807/buj.v1i2.24

[74] M. Shviro, D. Zitoun, RSC Adv. 3 (2013) 1380–1387. https://doi.org/10.1039/C2RA22024E

[75] Z. Zhang, X.-G. Wang, X. Zhang, Z. Xie, Y.-N. Chen, L. Ma, Z. Peng, Z. Zhou, Advanced Science. 5 (2018) 1700567. https://doi.org/10.1002/advs.201700567

[76] D. Wang, Y. Li, Advanced Materials, 23 (2011) 1044-1060. https://doi.org/10.1002/adma.201003695

[77] W.-J. Liu, T.-T. Qian, H. Jiang, Chemical Engineering Journal. 236 (2014) 448–463. https://doi.org/10.1016/j.cej.2013.10.062

[78] S. Sharafzadeh, J. Zolgharnein, A. Nezamzadeh–Ejhieh, S. D. Farahani, Int. J. Hydrogen Energy. 106 (2025) 1429–1442. https://doi.org/10.1016/j.ijhydene.2025.02.031

[79] D. Ayodhya, M. Venkatesham, A. Santoshi kumari, G. Bhagavanth Reddy, D. Ramkrishna, G. Veerabhadram, J. Exp. Nanosci. 11 (2016) 418-432. https://doi.org/10.1080/17458080.2015.1070312

[80] M. Dhanalakshmi, S. Lakshmi Prabavathi, K. Saravanakumar, B. Filip Jones, V. Muthuraj, Chemical Physics Letters. 745 (2020) 137285. https://doi.org/10.1016/j.cplett.2020.137285

[81] M. Aamir, I. Bibi, S. Ata, F. Majid, S. Kamal, N. Alwadai, M. Sultan, S. Iqbal, M. Aadil, M. Iqbal, Journal of Molecular Liquids. 322 (2021) 114895. https://doi.org/10.1016/j.molliq.2020.114895

[82] V. Manikandan, R. Elancheran, P. Revathi, P. Suganya, K. Krishnasamy, Bull Mater Sci. 43 (2020) 265. https://doi.org/10.1007/s12034-020-02227-y

[83] N. Omrani, A. Nezamzadeh-Ejhieh, Iran. J. Catal. *15* (2025) 1-17. https://doi.org/10.57647/j.ijc.2025.1502.15

[84] A. Yousefi, A. Nezamzadeh-Ejhieh, Iran. J. Catal. 11 (2021) 247-259. https://oiccpress.com/ijc/article/view/3600

[85] K. Anandalakshmi, J. Venugobal, V. Ramasamy, Appl Nanosci. 6 (2016) 399–408. https://doi.org/10.1007/s13204-015-0449-z

[86] G. R. Mavlankar, P. P. Baikar, D. N. Rangadal, A. Chavan, K. Malkhede, M. N. Bhatu, S. P. Patil, Carbohydrate Research. 559 (2025) 109737. https://doi.org/10.1016/j.carres.2025.109737

[87] P. Vijaya Kumar, A. Jafar Ahamed, M. Karthikeyan, SN Appl. Sci. 1 (2019) 1083. https://doi.org/10.1007/s42452-019-1113-0

[88] M. Vanaja, G. Annadurai, Appl Nanosci. 3 (2013) 217–223. https://doi.org/10.1007/s13204-012-0121-9